Electronic Supplementary Material (ESI) for Journal of Materials Chemistry A.
This journal is © The Royal Society of Chemistry 2023

# Ultramicroporous iron-isonicotinate MOFs combining size-exclusion kinetics and thermodynamics for efficient $CO_2/N_2$ gas separation

Isabel Abánades Lázaro,[a†] Eleni C. Mazarakioti,[a†] Eduardo Andres-Garcia,[a] Bruno J. C. Vieira,[b] João C. Waerenborgh,[b] Iñigo J. Vitórica-Yrezábal,[c] Mónica Giménez-Marqués,[a] and Guillermo Mínguez Espallargas*[a]

[a] Instituto de Ciencia Molecular (ICMol), Universidad de Valencia, c/ Catedrático José Beltrán, 2, 46980, Paterna, Spain

[b] Centro de Ciências e Tecnologias Nucleares, DECN, Instituto Superior Técnico, Universidade de Lisboa, 2695-066 Bobadela, LRS, Portugal.

[c] School of Chemistry, University of Manchester, Oxford Road, Manchester M13 9PL, United Kingdom

[†] These authors contributed equally to this work

# Supporting information

## Table of contents

# S.1. Synthesis

All reagents unless otherwise stated were obtained from commercial sources and were used without further purification.

## S.1.1 Synthesis of $[Fe_3O(CH_3COO)_6]ClO_4 \cdot 3H_2O$

The synthesis of $[Fe_3O(CH_3COO)_6]ClO_4 \cdot 3H_2O$ was performed following a reported protocol.[1] 1.1 g of $Fe^0$ (0.02 mol) were dissolved in 10 ml of water (MQ), 5.6 ml of $HClO_4$ (60 %) were added dropwise and the solution was stirred at 50-60 ºC during 2 hours. The blue solution was cooled down to room temperature and stirred overnight. Then, 3.5 ml of $H_2O_2$ (35 %) and 0.6 ml of water were added dropwise to the solution with an ice bath and the solution changed from blue to orange. Finally, 3.3 g of $Na(CH_3COO)$ (0.04 mol) were carefully added at 0-5 ºC to the solution which became dark reddish. The solution was collected in a Petri dish and dark red crystals of $[Fe_3O(CH_3COO)_6]ClO_4 \cdot 3H_2O$ appeared after slow evaporation at room temperature, which was collected by filtration. Single crystals were isolated and its structure determined by X-ray single crystal diffraction (*vide infra*). The purity of the crystals was analysed by PXRD and TGA (Figure S1).

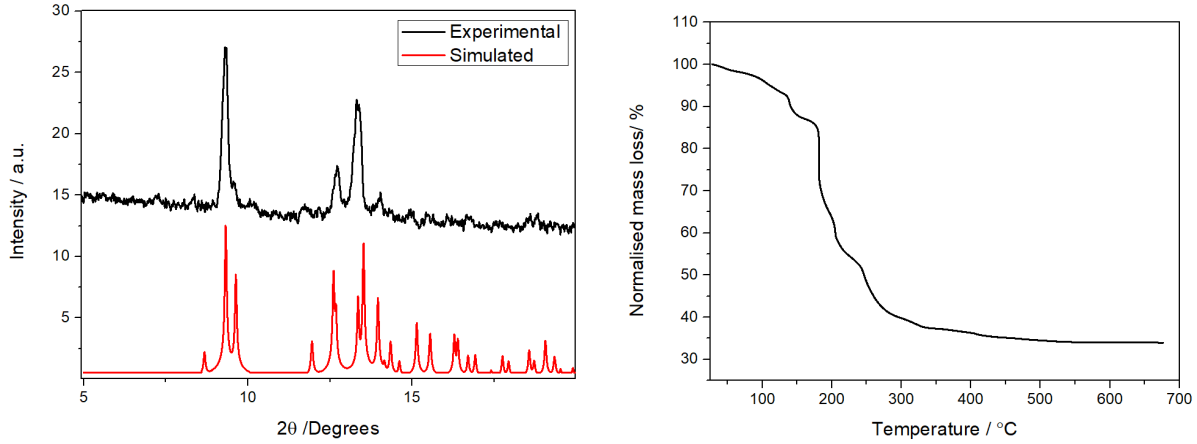


**Figure S1:** PXRD and TGA profile of $[Fe_3O(CH_3COO)_6]ClO_4 \cdot 3H_2O$. Theoretical TGA residue 34.6, experimental TGA residue 34.3.

## S.1.2 Synthesis of MUV-26α(DMF)

450 mg (0.65 mmol) of the preformed cluster $[Fe_3O(CH_3COO)_6]ClO_4 \cdot 3H_2O$ were dissolved in 41 mL of DMF in a 100 mL pyrex jar. Then, 923 mg of isonicotinic acid (7.5 mmol, 11.5 equivalents compared to cluster) were added to the solution and sonicated until complete dispersion (*ca*. 5 minutes). The dispersion was placed in an oven and heated to 120 °C, maintaining the temperature for 48 hours. The reaction was cooled down to room temperature and the precipitated crystals were washed with DMF (x5). For the activated sample, further washing with MeOH (x3) was performed, followed by overnight immersion in MeOH and activation at 150C under vacuum for 24 hours, yielding approximately 400 mg of crystals, corresponding to an approximate yield of *ca*. 44 %.

## S.1.3 Synthesis of MUV-26β(DMF)

691 mg (1 mmol) of the preformed cluster $[Fe_3O(CH_3COO)_6]ClO_4 \cdot 3H_2O$ were dissolved in 40 mL of DMF in a 100 mL pyrex jar. Then, 1.847 g of isonicotinic acid (15 mmol, 15 equivalents compared to cluster) were added to the solution and sonicated until complete dispersion (*ca*. 5 minutes). The dispersion was placed in an oven and heated to 120 °C, maintaining the temperature for 48 hours. The reaction was cooled down to room temperature and the precipitated crystals were washed with DMF (x5). For the activated sample, further washing with MeOH (x3) was performed, followed by overnight immersion in MeOH and activation at 150C under vacuum for 24 hours, yielding approximately 450 mg of crystals, corresponding to an approximate yield of ca. 49 %.

# S.2. Crystal structures

## S.2.1 Crystallographic information

**Data collection**: Single crystals of **MUV-26α(DMF), MUV-26α, MUV-26β(DMF)** and **MUV-26β** were mounted on glass fibers using a viscous hydrocarbon oil to coat the crystals and then transferred directly to the cold nitrogen stream for data collection. X-ray data were collected at 120 K on a Supernova diffractometer equipped with a graphite-monochromated Enhance (Mo) X-ray source (λ = 0.71073 Å). Data were measured using CrysAlisPro suite of programs. Single crystals of **MUV-26α($CS_2$)** and $[Fe_3O(CH_3COO)_6]ClO_4 \cdot 3H_2O$ were mounted mounted on glass fibers using a viscous hydrocarbon oil to coat the crystals and then transferred directly to the cold nitrogen stream for data collection. X-ray data were collected at 100 K on a DW rotating anode synergy R diffractometer with (Cu-kα) X-ray source (λ = 1.5406 Å). Data were measured using CrysAlisPro suite of programs.

**Crystal structure determinations and refinements**. The program CrysAlisPro, Oxford Diffraction Ltd., was used for unit cell determinations and data reduction. Empirical absorption correction was performed using spherical harmonics, implemented in the SCALE3 ABSPACK scaling algorithm, based upon symmetry-equivalent reflections combined with measurements at different azimuthal angles. The crystal structures were solved and refined against all $F^2$ values using the SHELX and Olex2 suite of programs.[2,3] All nonhydrogen atoms were refined anisotropically except in crystal structure of **MUV-26α** (i.e. the activated form of **MUV-26α(DMF)**), where 22 atoms were refined isotropically to maximize the data/parameter ratio. Hydrogen atoms were placed in calculated positions, refined using idealized geometries (riding model) and assigned fixed isotropic displacement parameters.

Despite the use of a highly intense microfocused X-ray source, crystals of **MUV-26α** only diffracted to 1.2 Å of resolution.

The remaining electron density in the pores of crystal structures of compounds **MUV-26β(DMF)**, and **MUV-26β** could not be assigned to any sensible chemical species and were accounted using solvent mask protocol implemented in OLEX2. 222 and 100 electrons in the unit cell were accounted for **MUV-26β(DMF)** and **MUV-26β** respectively, which could correspond to 1 DMF and 1 $H_2O$ per formula unit for compound **MUV-26β(DMF)**, and 0.5 DMF and 0.5 $H_2O$ per formula unit for compound **MUV-26β.**

Uncoordinated pyridyl groups in all crystal structures were disordered and modelled over two positions. Disordered DMF molecules in **MUV-26α(DMF)** and $CS_2$ molecules in **MUV-26α($CS_2$)** were modelled as rigid bodies over two positions. C–N and C–C bonds were restrained to be similar using SHELX bond restraint commands (SADI). The atomic displacement parameters were also restrained to have similar values using similar values (SIMU) and rigid body restraints (RIGU) in SHELX.

Occupancy of $CS_2$ molecules in **MUV-26α($CS_2$)** were refined showing the presence of 0.9 and 0.3 $CS_2$ molecules in the asymmetric unit. C–S bond distances were restrained to be equal using SADI (SHELX) commands.

CCDC 2217199–2217202 and 2237339–2237340 contain the supplementary crystallographic data for this paper. These data can be obtained free of charge via www.ccdc.cam.ac.uk/conts/retrieving.html (or from the Cambridge Crystallographic Data Centre, 12 Union Road, Cambridge CB21EZ, UK; fax: (+44)1223-336-033; or deposit@ccdc.cam.ac.uk).

**Table S1.** Crystallographic information of compounds **MUV-26α(DMF)**, **MUV-26β(DMF)**, **MUV-26α** and **MUV-26β**

| Identification code | **MUV26α(DMF)** | **MUV26β(DMF)** | **MUV26α** | **MUV26β** |
|---|---|---|---|---|
| Empirical formula | $C_{42}H_{38}Fe_3N_8O_{15}$ | $C_{36}H_{25}Fe_3N_6O_{13.5}$ | $C_{36}H_{24}Fe_3N_6O_{13}$ | $C_{36}H_{25}Fe_3N_6O_{13.5}$ |
| Formula weight | 1062.35 | 925.17 | 916.16 | 925.17 |
| Temperature/K | 120(1) | 120(1) | 120(1) | 120(1) |
| Crystal system | orthorhombic | monoclinic | orthorhombic | monoclinic |
| Space group | *Pnma* | $P2_1$ | *Pnma* | $P2_1$ |
| *a*/Å | 20.5173(8) | 10.3799(7) | 20.0962(16) | 10.4288(6) |
| *b*/Å | 19.3490(5) | 21.7382(10) | 19.1224(7) | 21.5963(9) |
| *c*/Å | 11.4667(3) | 20.9849(10) | 11.6431(4) | 20.9083(12) |
| *α*/° | 90 | 90 | 90 | 90 |
| *β*/° | 90 | 102.392(6) | 90 | 101.909(5) |
| *γ*/° | 90 | 90 | 90 | 90 |
| Volume/Å$^3$ | 4552.2(2) | 4624.7(4) | 4474.3(4) | 4607.7(4) |
| Z | 4 | 4 | 4 | 4 |
| $\rho_{calc}$/g·cm$^{-3}$ | 1.550 | 1.329 | 1.360 | 1.334 |
| μ/mm$^{-1}$ | 1.021 | 0.991 | 1.023 | 0.995 |
| F(000) | 2176.0 | 1876.0 | 1856.0 | 1876.0 |
| Crystal size/mm$^3$ | 0.23 × 0.21 × 0.15 | 0.15 × 0.13 × 0.12 | 0.17 × 0.13 × 0.11 | 0.15 × 0.13 × 0.12 |
| Radiation | Mo $K_\alpha$ ($\lambda$ = 0.71073) | Mo $K_\alpha$ ($\lambda$ = 0.71073) | Mo $K_\alpha$ ($\lambda$ = 0.71073) | Mo $K_\alpha$ ($\lambda$ = 0.71073) |
| 2Θ range for data collection/° | 5.73 to 50.048 | 6.436 to 50.048 | 5.764 to 34.45 | 5.974 to 50.054 |
| Index ranges | –24 ≤ h ≤ 24<br>–23 ≤ k ≤ 22<br>–13 ≤ l ≤ 9 | –12 ≤ h ≤ 12<br>–25 ≤ k ≤ 25<br>–24 ≤ l ≤ 24 | –16 ≤ h ≤ 16<br>–15 ≤ k ≤ 15<br>–9 ≤ l ≤ 9 | –11 ≤ h ≤ 12<br>–25 ≤ k ≤ 25<br>–23 ≤ l ≤ 24 |
| Reflections collected | 15219 | 81339 | 42082 | 32909 |
| Independent reflections | 4143 [$R_{int}$ = 0.1088, $R_{sigma}$ = 0.1341] | 16312 [$R_{int}$ = 0.1631, $R_{sigma}$ = 0.1713] | 1408 [$R_{int}$ = 0.1556, $R_{sigma}$ = 0.0398] | 16257 [$R_{int}$ = 0.1158, $R_{sigma}$ = 0.2599] |
| Data/restraints/parameters | 4143/1182/493 | 16312/2422/1248 | 1408/0/174 | 16257/2528/1263 |
| Goodness-of-fit on $F^2$ | 1.037 | 0.982 | 1.127 | 0.978 |
| Final R indexes [I>=2σ (I)] | $R_1$ = 0.0967, $wR_2$ = 0.2165 | $R_1$ = 0.0776, $wR_2$ = 0.1603 | $R_1$ = 0.0694, $wR_2$ = 0.1729 | $R_1$ = 0.0915, $wR_2$ = 0.1575 |
| Final R indexes [all data] | $R_1$ = 0.1541, $wR_2$ = 0.2578 | $R_1$ = 0.1393, $wR_2$ = 0.1941 | $R_1$ = 0.0877, $wR_2$ = 0.1854 | $R_1$ = 0.1868, $wR_2$ = 0.2005 |
| Largest diff. peak/hole / e Å$^{-3}$ | | 0.69/–0.48 | | 0.69/–0.45 |

**Table S2.** Crystallographic information of compounds **MUV-26α($CS_2$)** and **$[Fe_3O(CH_3COO)_6]ClO_4 \cdot {}_3H_2O$**

| Identification code | **MUV-26α($CS_2$)** | **$[Fe_3O(CH_3COO)_6]ClO_4 \cdot 3H_2O$** |
|---|---|---|
| Empirical formula | $C_{37.55}H_{24}Fe_3N_6O_{13}S_{3.11}$ | $C_{12}H_{30}ClFe_3O_{23}$ |
| Formula weight | 1034.54 | 745.36 |
| Temperature/K | 120(1) | 120(1) |
| Crystal system | orthorhombic | monoclinic |
| Space group | *Pnma* | $P2_1/c$ |
| *a*/Å | 20.5085(19) | 13.31407(16) |
| *b*/Å | 19.1512(7) | 14.79814(13) |
| *c*/Å | 11.5528(4) | 15.13991(18) |
| *α*/° | 90 | 90 |
| *β*/° | 90 | 112.0380(14) |
| *γ*/° | 90 | 90 |
| Volume/Å$^3$ | 4537.5(5) | 2764.97(6) |
| Z | 4 | 4 |
| $\rho_{calc}$/g·cm$^{-3}$ | 1.514 | 1.791 |
| μ/mm$^{-1}$ | 9.506 | 14.225 |
| F(000) | 2092.0 | 1524.0 |
| Crystal size/mm$^3$ | 0.04 × 0.01 × 0.01 | 0.19 × 0.16 × 0.15 |
| Radiation | CuK$_\alpha$ ($\lambda$ = 1.54184) | Cu K$_\alpha$ ($\lambda$ = 1.54184) |
| 2Θ range for data collection/° | 8.624 to 136.482 | 7.162 to 153.704 |
| Index ranges | -24 ≤ h ≤ 24, -20 ≤ k ≤ 23, -13 ≤ l ≤ 13 | -16 ≤ h ≤ 16, -18 ≤ k ≤ 18, -18 ≤ l ≤ 18 |
| Reflections collected | 16030 | 41083 |
| Independent reflections | 4289 [$R_{int}$ = 0.1059, $R_{sigma}$ = 0.0855] | 5713 [$R_{int}$ = 0.0309, $R_{sigma}$ = 0.0165] |
| Data/restraints/parameters | 4289/360/417 | 5713/2/375 |
| Goodness-of-fit on F$^2$ | 1.075 | 1.049 |
| Final R indexes [I>=2σ (I)] | $R_1$ = 0.1406, w$R_2$ = 0.3414 | $R_1$ = 0.0231, w$R_2$ = 0.0596 |
| Final R indexes [all data] | $R_1$ = 0.1821, w$R_2$ = 0.3644 | $R_1$ = 0.0238, w$R_2$ = 0.0599 |
| Largest diff. peak/hole / e Å$^{-3}$ | 1.48/-0.84 | 0.65/-0.59 |

## S.2.2 Crystal structure of MUV-26α(DMF)

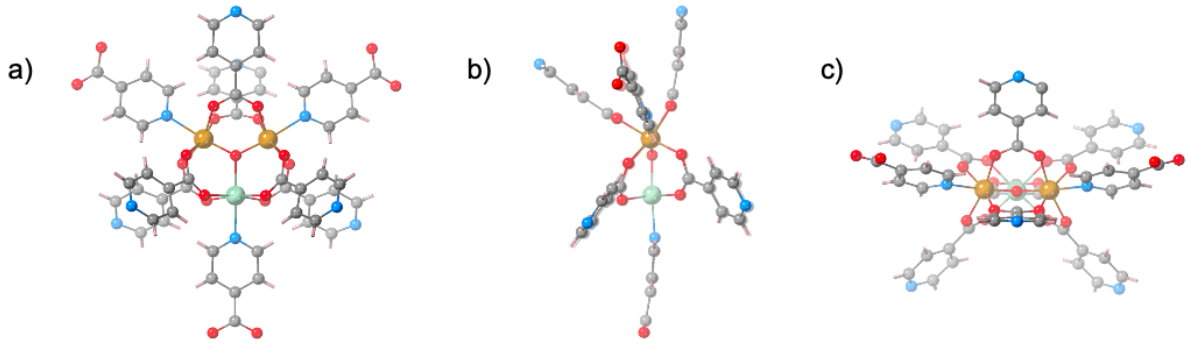


**Figure S2:** Trinuclear SBU of **MUV-26α(DMF)**, shown in three orthogonal views.

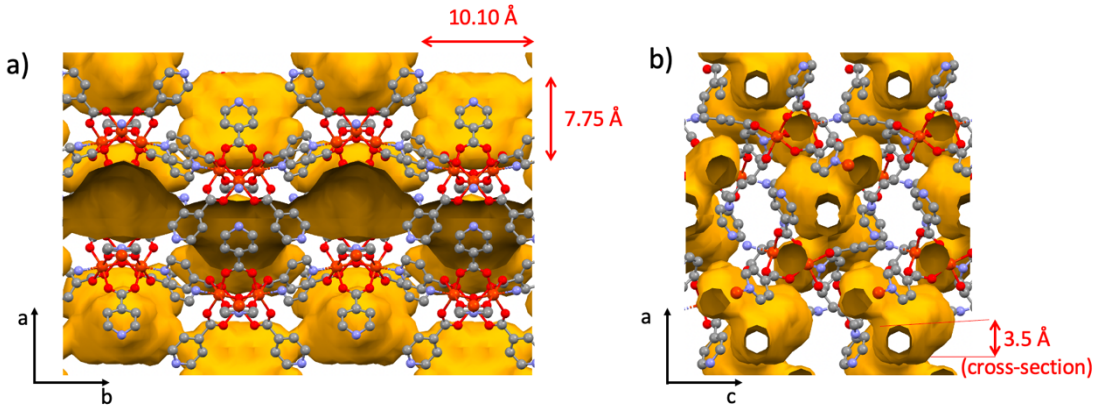


**Figure S3**. Crystal structure of **MUV-26-α**, showing the dimensions of the pores.

## S.2.3 Crystal structure of MUV-26β(DMF)

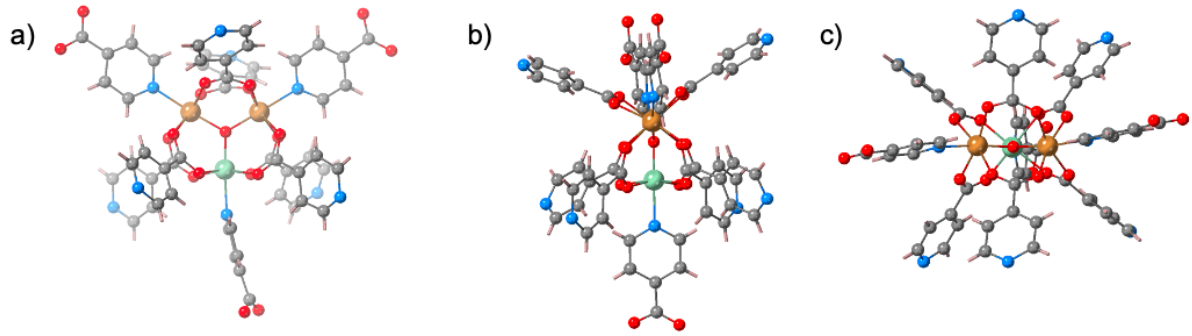


**Figure S4:** Trinuclear SBU (cluster 1) of **MUV-26β(DMF)**, shown in three orthogonal views.

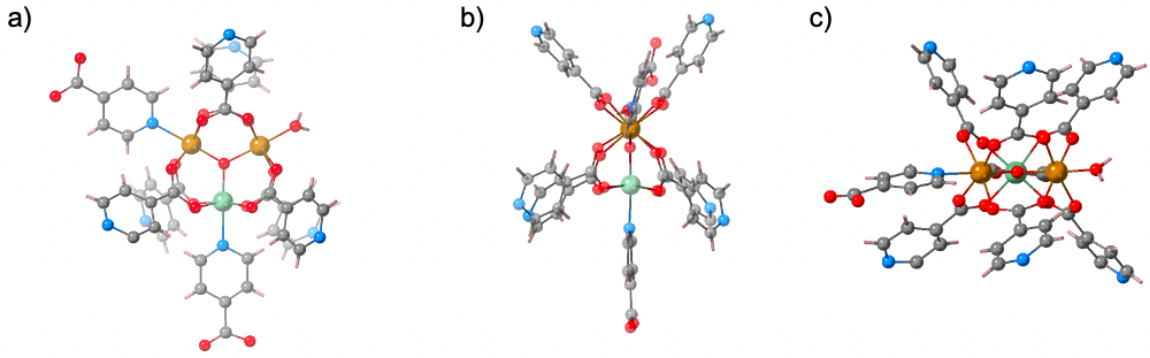


**Figure S5:** Trinuclear SBU (cluster 2) of **MUV-26β(DMF)**, shown in three orthogonal views.

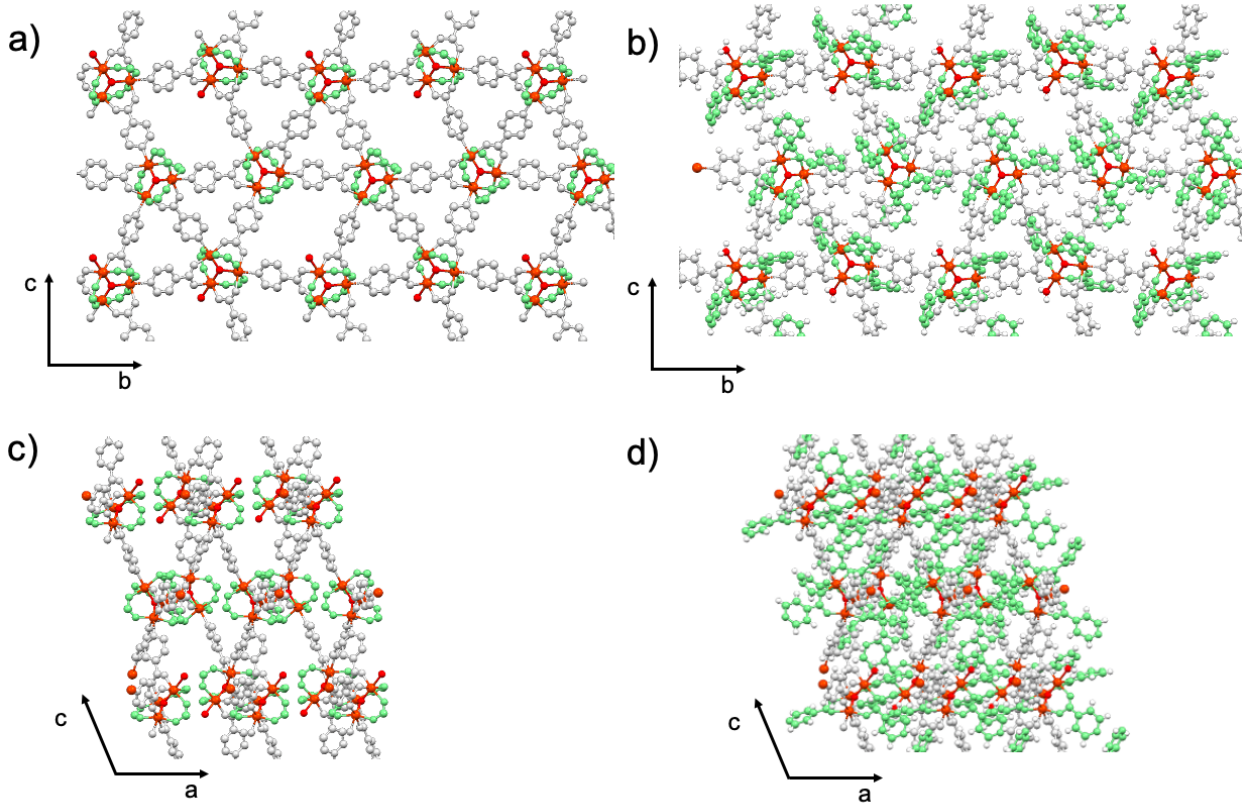


**Figure S6:** Crystal structure of **MUV-26β(DMF)** along *a*- and *b*- axes. The pendant pyridyl groups are shown in green (omitted in Figures S6a and S6c to clearly show the 3D network), whereas the bridging isonicotinate ligands are shown in white and the trimetallic SBU is shown in red.

## S.2.4 Bond valance sum calculations

Bond valence sum calculations were performed using the structural information from single-crystal diffraction data.

**Table S3:** Bond valance sums calculations for **MUV-26α(DMF)**.

| Fe | atom label | bond distance | | Fe(II) | Fe(III) |
|---|---|---|---|---|---|
| **Fe1** | O1 | 1.841 | O | 0.6831 | 0.8012 |
| | O3 | 2.023 | O | 0.4177 | 0.4899 |
| | O5 | 2.025 | O | 0.4155 | 0.4873 |
| | O6 | 2.052 | O | 0.3862 | 0.4530 |
| | O7 | 2.051 | O | 0.3873 | 0.4542 |
| | N12 | 2.237 | N | 0.2823 | 0.2748 |
| | | | | 2.5721 | **2.9604** |
| **Fe2** | O1 | 2.036 | O | 0.4033 | 0.4730 |
| | O2 | 2.102 | O | 0.3374 | 0.3957 |
| | O2 | 2.102 | O | 0.3374 | 0.3957 |
| | O4 | 2.179 | O | 0.2740 | 0.3214 |
| | O4 | 2.179 | O | 0.2740 | 0.3214 |
| | N24 | 2.186 | N | 0.3240 | 0.3154 |
| | | | | **1.9501** | 2.2226 |

Note that there are two crystallographically equivalent Fe(III)

**Table S4:** Bond valance sum calculations for cluster 1 of **MUV-26β(DMF)**.

| Fe | atom label | bond distance | | Fe(II) | Fe(III) |
|---|---|---|---|---|---|
| **Fe1** | O1 | 1.850 | O | 0,6667 | 0,782 |
| | O3 | 2.018 | O | 0,4234 | 0,4966 |
| | O5 | 1.974 | O | 0,4769 | 0,5593 |
| | O6 | 2.034 | O | 0,4055 | 0,4756 |
| | O8 | 2.049 | O | 0,3894 | 0,4567 |
| | N75 | 2.217 | N | 0,2980 | 0,2900 |
| | | | | 2,6597 | **3,0601** |
| **Fe2** | O1 | 1.987 | O | 0,4604 | 0,5400 |
| | O2 | 2.148 | O | 0,298 | 0,3495 |
| | O4 | 2.099 | O | 0,3401 | 0,3990 |
| | O10 | 2.116 | O | 0,3249 | 0,3810 |
| | O12 | 2.115 | O | 0,3258 | 0,3821 |
| | N47 | 2.158 | N | 0,3495 | 0,3401 |
| | | | | **2,0986** | 2,3916 |
| **Fe3** | O1 | 1.878 | O | 0,6181 | 0,7250 |
| | O7 | 2.033 | O | 0,4066 | 0,4769 |
| | O9 | 2.061 | O | 0,3769 | 0,4421 |
| | O11 | 2.005 | O | 0,4385 | 0,5143 |
| | O13 | 2.001 | O | 0,4433 | 0,5199 |
| | N5 | 2.201 | N | 0,3111 | 0,3028 |
| | | | | 2,5946 | **2,9810** |

**Table S5:** Bond valance sums calculations for cluster 2 of **MUV-26β(DMF)**.

| Fe | atom label | bond distance | | Fe(II) | Fe(III) |
|---|---|---|---|---|---|
| **Fe4** | O14 | 1.842 | O | 0,6813 | 0,7991 |
| | O15 | 1.974 | O | 0,4769 | 0,5593 |
| | O17 | 2.033 | O | 0,4066 | 0,4769 |
| | O19 | 2.005 | O | 0,4385 | 0,5143 |
| | O23 | 1.991 | O | 0,4554 | 0,5342 |
| | N26 | 2.208 | N | 0,3053 | 0,2972 |
| | | | | 2,7640 | **3,1809** |
| **Fe5** | O14 | 1.916 | O | 0,5578 | 0,6542 |
| | O18 | 2.150 | O | 0,2963 | 0,3476 |
| | O20 | 2.120 | O | 0,3214 | 0,3769 |
| | O21 | 2.033 | O | 0,4066 | 0,4769 |
| | O26 | 2.031 | O | 0,4088 | 0,5920 |
| | O27 | 2.092 | O | 0,3466 | 0,5020 |
| | | | | 2,3375 | **2,9495** |
| **Fe6** | O14 | 1.944 | O | 0,5171 | 0,6065 |
| | O16 | 2.110 | O | 0,3302 | 0,3873 |
| | O22 | 2.132 | O | 0,3111 | 0,3649 |
| | O24 | 2.081 | O | 0,3571 | 0,4188 |
| | O25 | 2.062 | O | 0,3759 | 0,5444 |
| | N61 | 2.176 | N | 0,2762 | 0,4000 |
| | | | | **2,1677** | 2,7220 |

## S2.5 $CS_2$ adsorption by MUV-26α

Crystals of **MUV-26α** were soaked for 1 day in $CS_2$. Crystal structure of $CS_2$ containing **MUV-26α($CS_2$)** shows the presence of 1.55 molecules of $CS_2$ per formula unit. $CS_2$ guest molecules were found in two different crystallographic positions with an 90 % occupancy for position 1 and 30 % occupancy for position 2. $CS_2$ at position 2 were found disordered with a symmetrically equivalent $CS_2$ molecule. Both crystallographically independent $CS_2$ molecules were found in the interlayer space of the **MUV-26α** polymers. Both $CS_2$ molecules formed S···H–C hydrogen bonds with the highly disordered nicotinate ligands and S···C–O contacts with the carbons of the carboxylate groups.

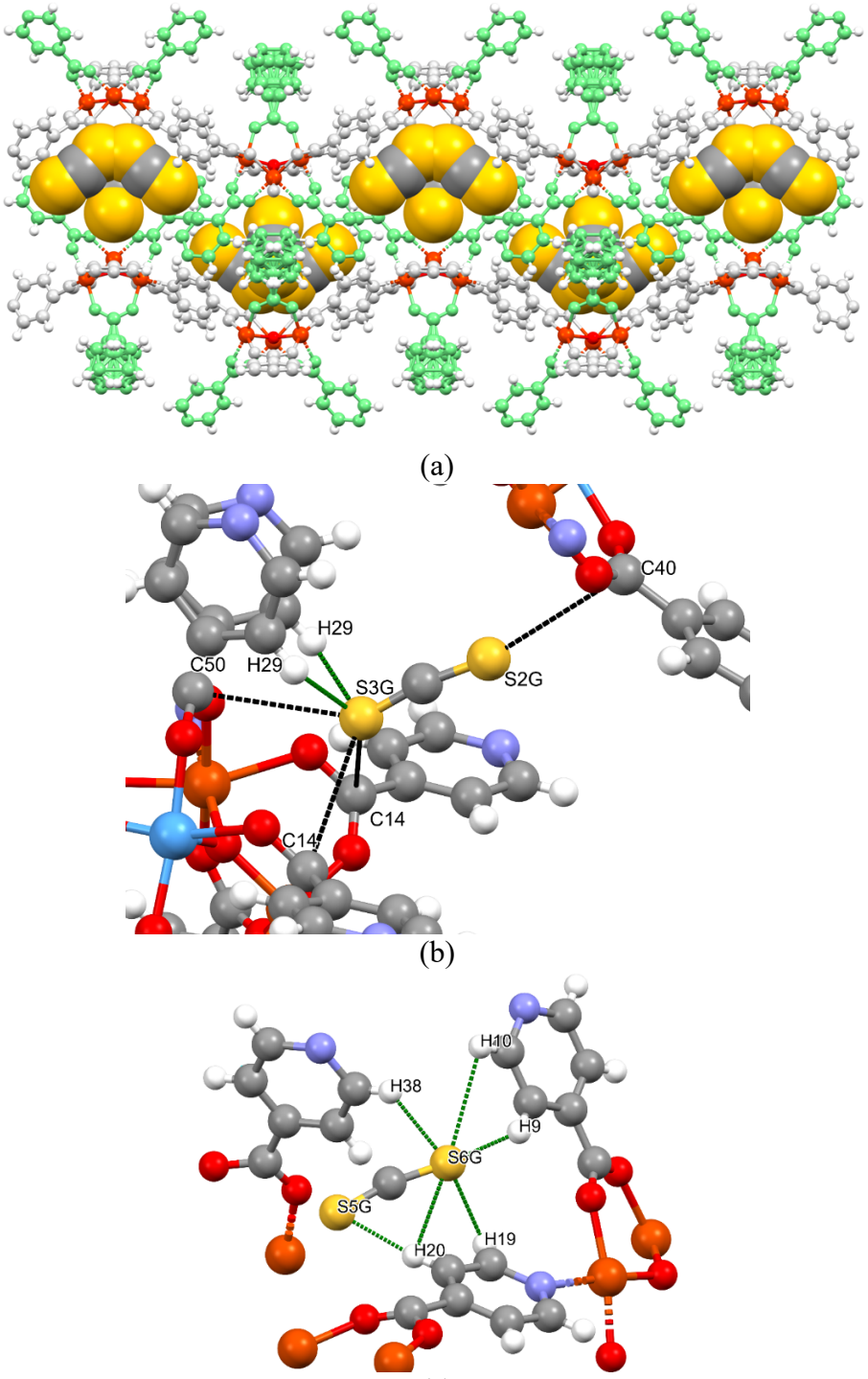


**Figure S7:** a) Crystal structure of **MUV-26α($CS_2$)** along *c* axes. The pendant pyridyl groups are shown in green whereas the bridging isonicotinate ligands are shown in white, the $CS_2$ are shown in orange(S)/grey(C) and the trimetallic SBU is shown in red. The interactions between the $CS_2$ molecules in positions 1and 2 are shown in b) and c), respectively. Iron shown in orange, oxygens red, sulphur in orange, carbons in grey and hydrogen in white. Hydrogen bonds contacts are shown in green and S···C–O contacts in black.

**Table S6.** Intermolecular interactions between $CS_2$ and and **MUV-26α**

| $CS_2$ atom | **MUV-26α($CS_2$)** atom | Diastance (Å) |
|---|---|---|
| S3G | H29 | 1.96 |
| S3G | C14 | 3.54(4) |
| S3G | C50 | 3.51(3) |
| S2G | C40 | 3.45(3) |
| S5G | H20 | 2.19 |
| S6G | H9 | 1.97 |
| S6G | H10 | 2.99 |
| S6G | H19 | 2.34 |
| S6G | H20 | 2.19 |
| S6G | H38 | 2.32 |

# S.3. Chemical characterization

## S.3.1 Microscope images of crystals

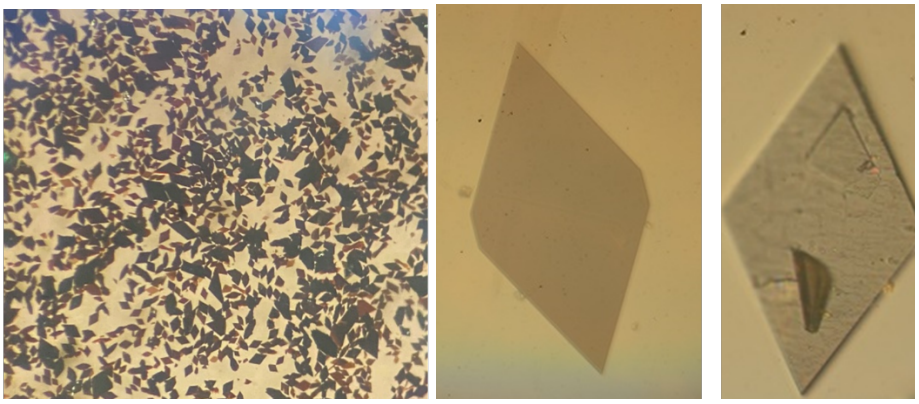

**Figure S8.** Optical microscope images of **MUV-26α**.

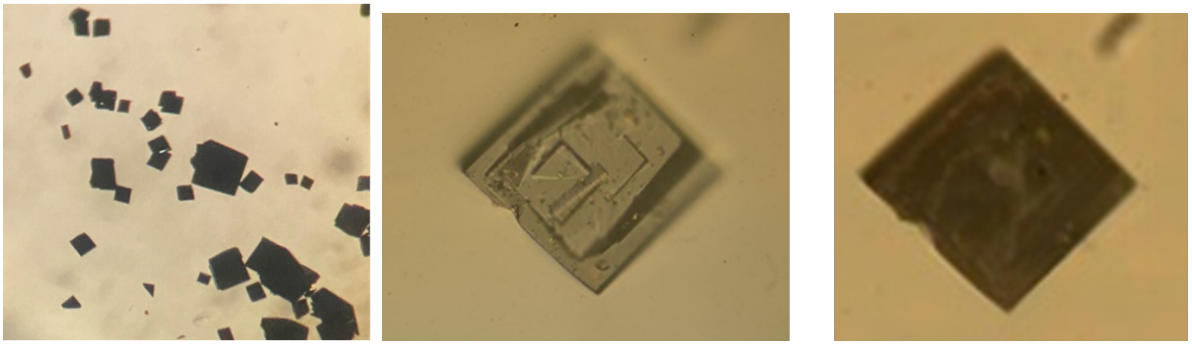

**Figure S9.** Optical microscope images of **MUV-26β**.

## S.3.2 Scanning Electron Microscopy and energy-dispersive X-ray analysis

Scanning Electron Microscopy (SEM) and single point energy-dispersive X-ray analysis (EDX): particle morphologies, dimensions and mapping were studied with a Hitachi S-4800 scanning electron microscope at an accelerating voltage of 20 kV.

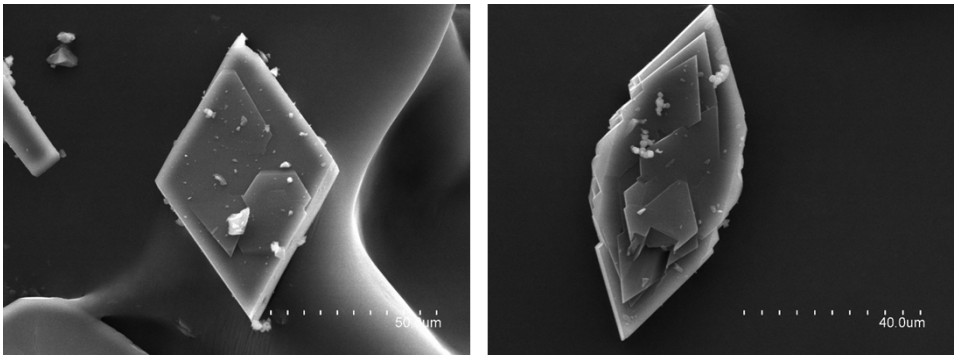


**Figure S10.** Scanning electron microscope images of **MUV-26α**.

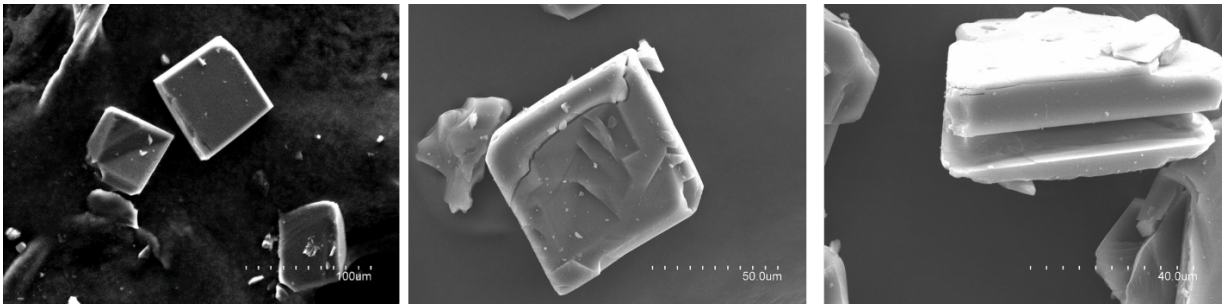


**Figure S11.** Scanning electron microscope images of **MUV-26β**.

## S.3.3 Powder X-ray diffraction

Powder X-ray diffraction (PXRD) patterns were recorded using 0.7 mm borosilicate capillaries that were aligned on an Empyrean PANalytical powder diffractometer, using Cu $K_\alpha$ radiation ($\lambda$ = 1.54056 Å) with a PIXcel detector.

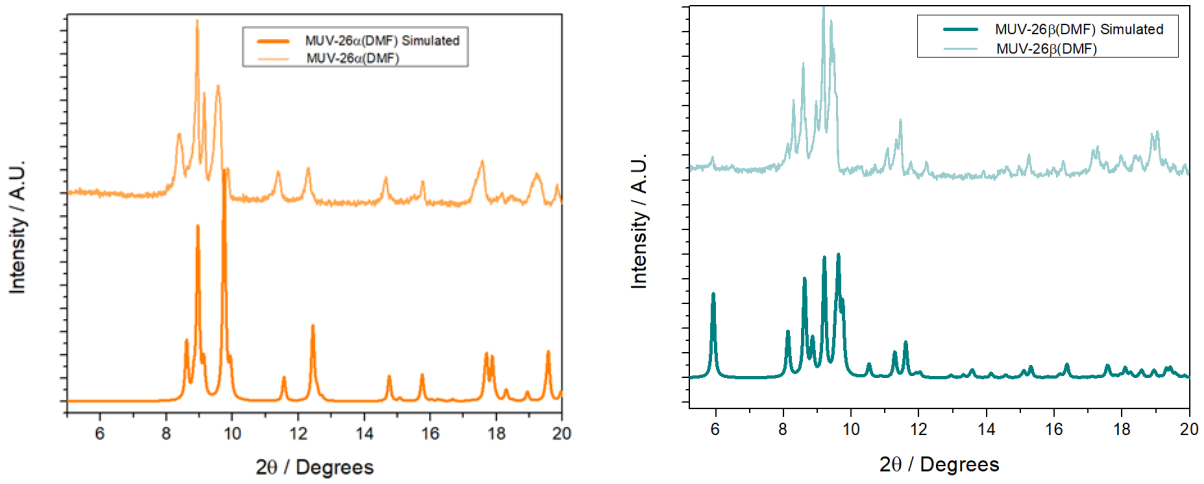


**Figure S12.** Comparison of experimental and simulated PXRD pattern of **MUV-26α(DMF)** and **MUV-26β(DMF).**

## S.3.4 Mössbauer Spectroscopy

Mössbauer spectra of **MUV-26α(DMF)** and **MUV-26β(DMF)** samples were collected at 4 K in transmission mode using a conventional constant-acceleration spectrometer and a 25 mCi $^{57}$Co source in a Rh matrix. The velocity scale was calibrated using α-Fe foil. Isomer shifts, IS, are given relative to this standard at room temperature. The absorbers were obtained by gently packing the samples into perspex holders. Absorber thickness was calculated on the basis of the corresponding electronic mass-absorption coefficients for the 14.4 keV radiation, according to Long *et al.*[4] The low-temperature measurements were performed in a bath cryostat with the sample immersed in liquid He at 4 K. The spectra were fitted to Lorentzian lines using a non-linear least-squares method.[5]

The spectra consist of two quadrupole doublets. The estimated parameters for the doublets with lower IS and quadrupole splittings are typical of $Fe^{3+}$ and for the remaining doublets typical of $Fe^{2+}$.[6]

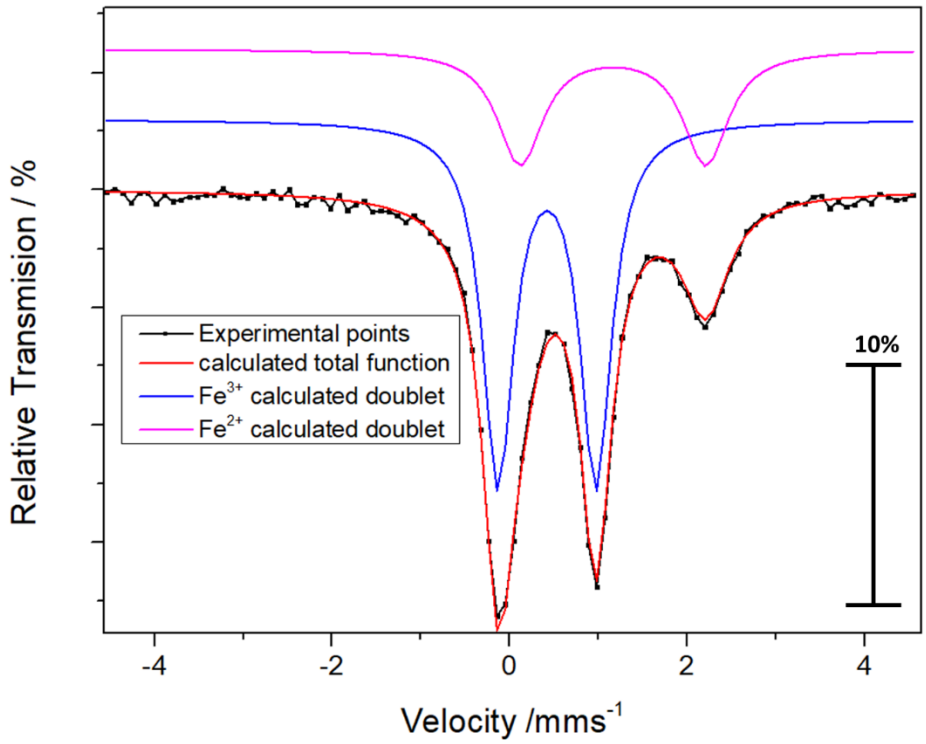


**Figure S13.** Mössbauer spectra at 4 K of **MUV-26α(DMF)**. The red line over the experimental points are the sum of two doublets.

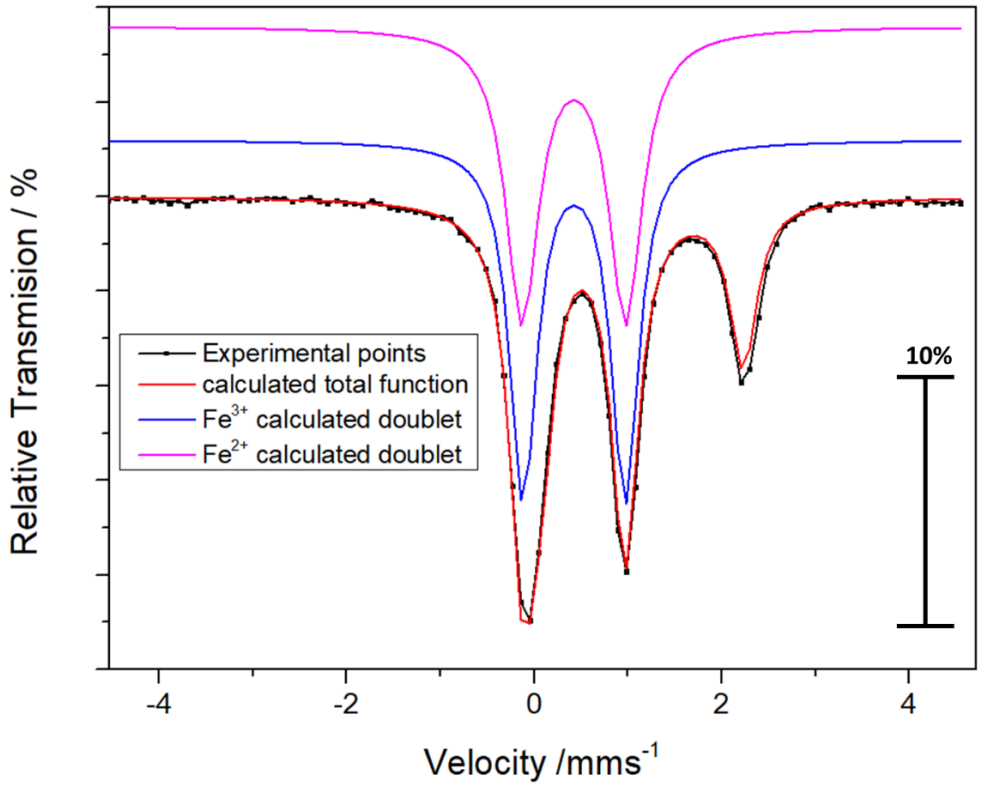


**Figure S14.** Mössbauer spectra at 4 K of **MUV-26β(DMF)**.

**Table S7.** Estimated parameters from the Mössbauer spectra of **MUV-26**.

| Sample | Fe oxidation state | Isomer shift (mm/s) | Quadrupole splitting (mm/s) | Γ | I |
|---|---|---|---|---|---|
| **MUV-26α(DMF)** | $Fe^{3+}$ | 0.53 | 1.10 | 0.42 | 68 % |
| | $Fe^{2+}$ | 1.28 | 2.09 | 0.61 | 32 % |
| **MUV-26β(DMF)** | $Fe^{3+}$ | 0.54 | 1.09 | 0.35 | 68 % |
| | $Fe^{2+}$ | 1.27 | 2.17 | 0.34 | 32 % |

Isomer shift relative to metallic α-Fe at 295 K. Estimated errors ≤ 0.02 mm/s for IS and QS and <2% for I.

## S.3.5 Thermogravimetric analysis

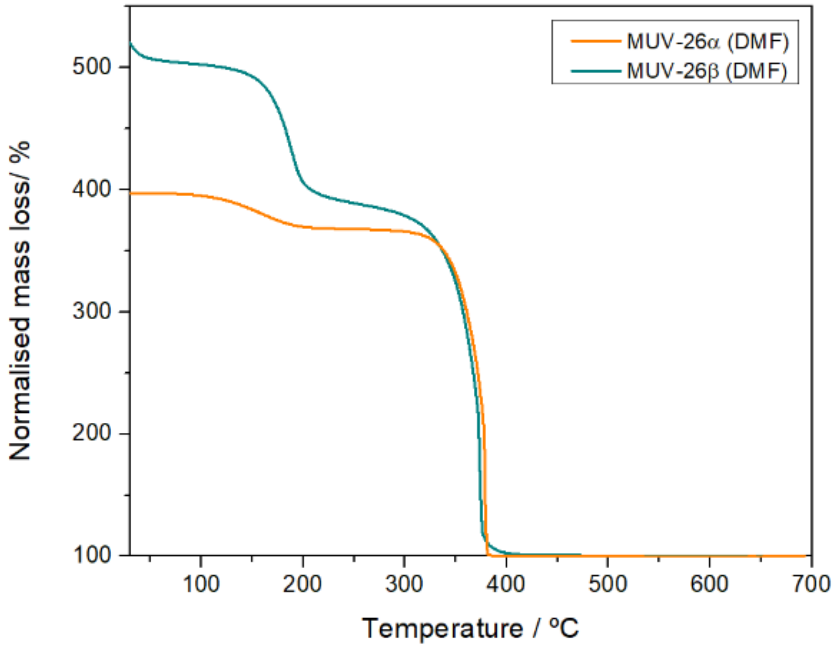


**Figure S15:** TGA of as synthesised materials after drying at RT from DMF solution, with the start of the decomposition profile normalised to 100% showing the high DMF content of the samples.

# S.4. Gas adsorption studies

## S.4.1. Activation

The precipitated crystals were washed with DMF (x5) and with MeOH (x3), then immersed in MeOH for 24 hours and further washed with methanol 3 times. The samples were dried under vacuum at 150 ºC for 24 hours.

Activated materials were characterized by XRPD, FTIR and TGA. Digested samples were characterized by $^{1}$H NMR to quantify the amount of solvent left in the pores.

FTIR spectra of solids were collected using a Shimadzu Fourier Transform Infrared Spectrometer, FTIR-8400S, fitted with a Diamond ATR unit.

TGA were carried out with a Mettler Toledo TGA/SDTA 851 apparatus between 25 and 700 °C under ambient conditions (10 °C·min$^{-1}$ scan rate and an airflow of 9 mL·min$^{-1}$).

$^{1}$H NMR spectra were recorded on a Bruker AVIII 300 MHz spectrometer and referenced to residual solvent peaks, using approximately 5 mg of MOF that were digested in 0.6 mL of d$^{6}$-DMSO with 5 drops of $D_2SO_4$ and heating at 75 °C and stirring until complete dissolution.

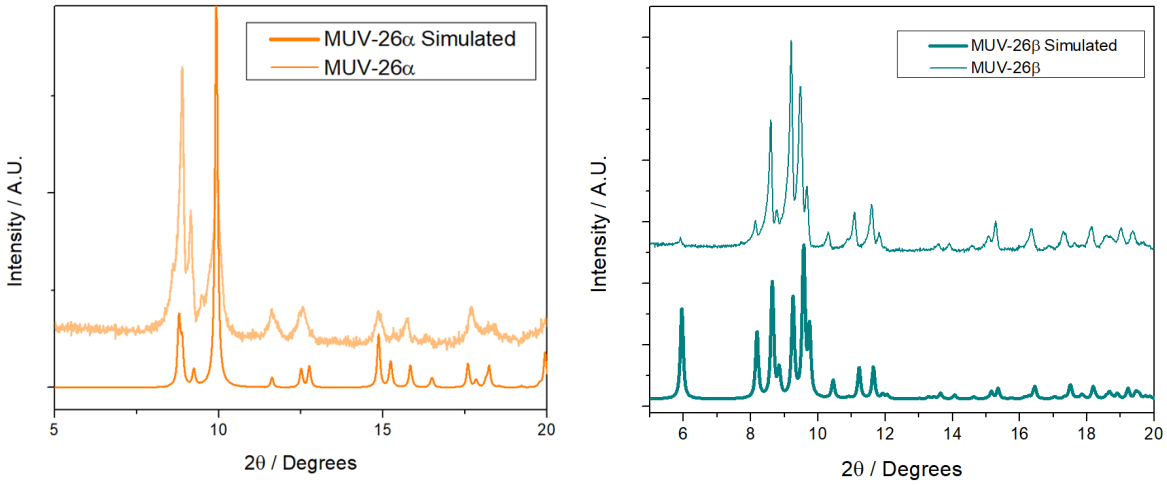


**Figure S16.** Experimental and simulated PXRD pattern of **MUV-26α** and **MUV-26β**.

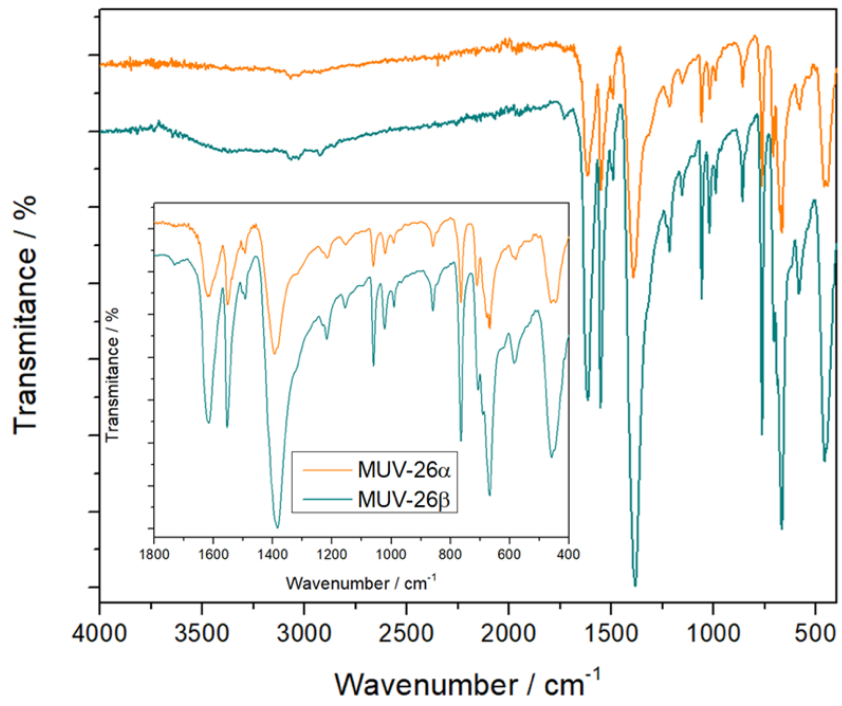


**Figure S17.** Comparison of the FT-IR spectra of **MUV-26α** and **MUV-26β**, showing almost identical vibration bands.

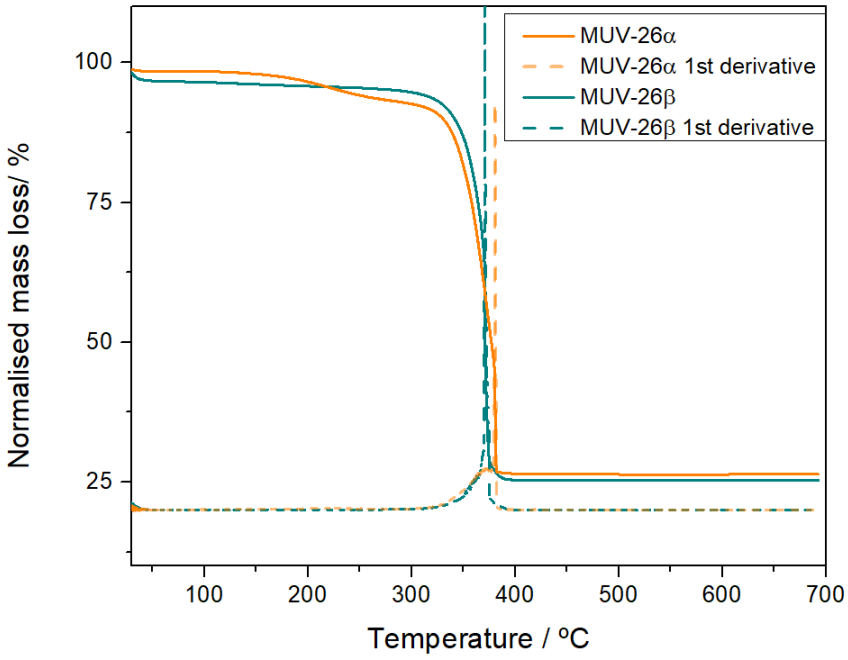


**Figure S18.** TGA profiles of **MUV-26α** and **MUV-26β** activated at 150 ºC.

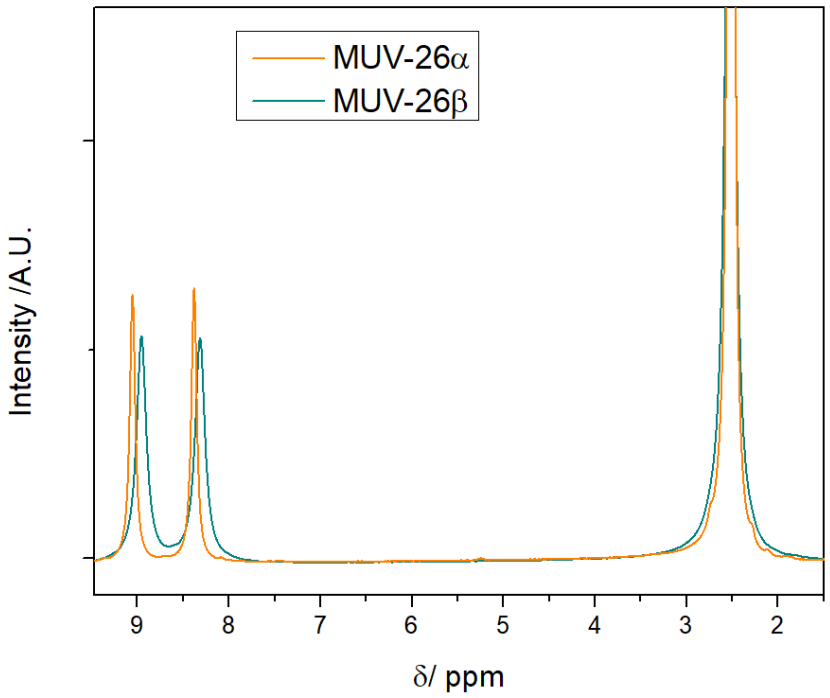


**Figure S19.** Comparison the acid-digested $^{1}$H NMR spectra of **MUV-26α** and **MUV-26β** activated at 150 ºC.

## S.4.2. Low-pressure studies

Low-pressure adsorption isotherms of $N_2$ and $CO_2$ were performed in a Tristar II Plus Micromeritics sorptometer, at 77 K and 273 K, respectively. Activation was set at 393 K, under vacuum, for 2 hours on the already activated samples at 150°C (see previous activated conditions).

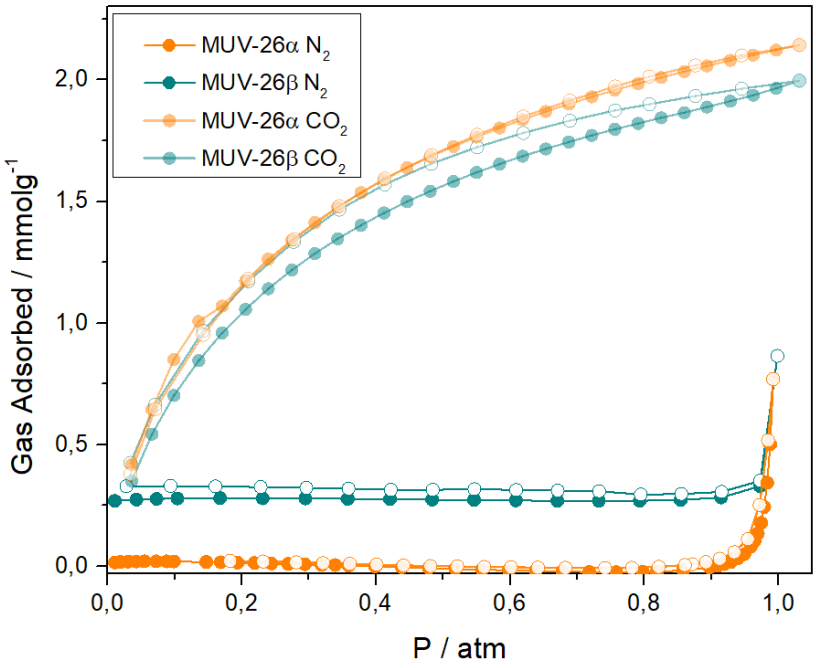


**Figure S20.** Comparison of the $N_2$ and $CO_2$ adsorption and desorption isotherms of **MUV-26α** and **MUV-26β** (at 77 K and 273 K, respectively), suggesting that these materials could be optimal for $N_2/CO_2$ separation.

**Table S8.** Calculation of the number of molecules of $CO_2$ per g of material and number of mol of $CO_2$ per mol of material.

| | $CO_2$ adsorbed (mmol/g) | mol $CO_2$/ mol MOF |
|---|---|---|
| **MUV-26α** | 2.1 | 7.9 |
| **MUV-26β** | 2.0 | 7.4 |

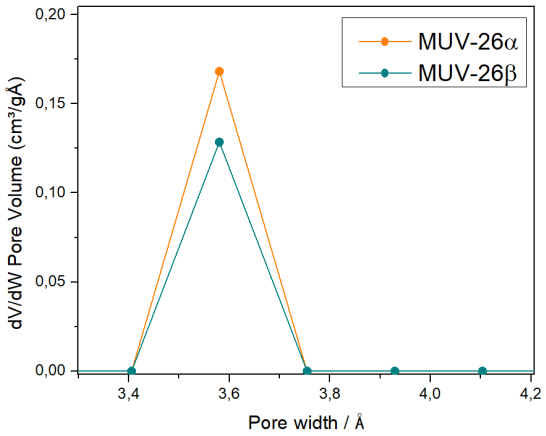


**Figure S21:** Comparison of the pore size distribution extracted from the $CO_2$ adsorption isotherms of **MUV-26α** and **MUV-26β** activated 150 ºC, using the $CO_2$@273 Carbon NLDFT pore model.

## S.4.3. High-pressure studies

High-pressure adsorption isotherms of $CO_2$ were measured at different temperatures ranging from 283 to 333 K in an IGA-001 gravimetric single component gas sorption analyser (Hiden Isochema) using approximately 100 mg of sample. Before each adsorption experiment, the sample was outgassed at 423 K under a vacuum ($10^{-5}$ Pa) for two hours. The sample was then cooled down, still under high vacuum, to the target temperature that was controlled using a recirculating thermostatic bath. Equilibrium conditions corresponded to 600 s interval, and 0.001 mg·min$^{-1}$ tolerance. Virial equations were applied for fitting experimental data points with a fourth-grade polynomial used to properly describe the $CO_2$ isotherms. The heat of adsorption was calculated according to the Clausius–Clapeyron equation through the data extracted from the experimental isotherms at different temperatures.

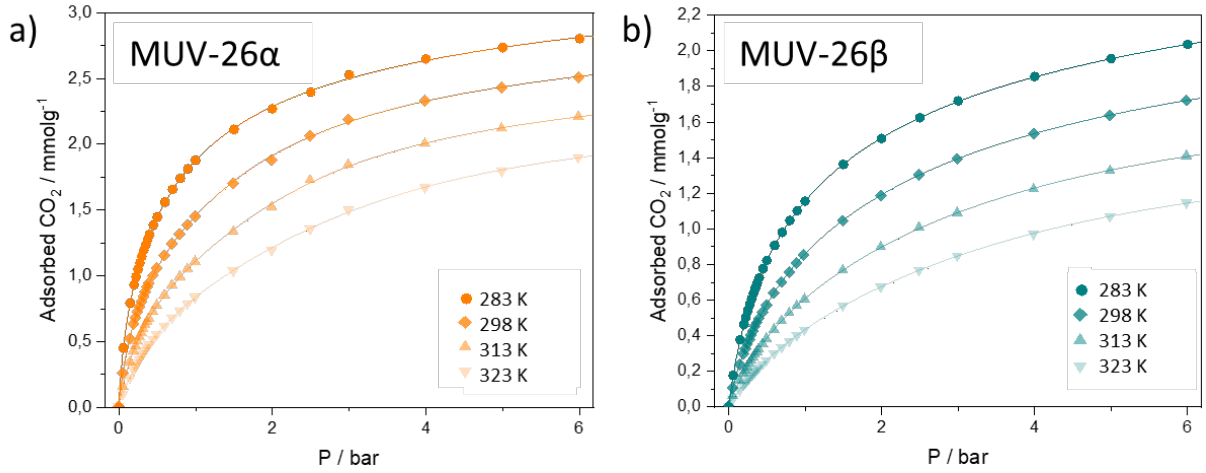


**Figure S22.** Comparison of the high-pressure $CO_2$ adsorption and desorption isotherms of **MUV-26α** and **MUV-26β** at different temperatures.

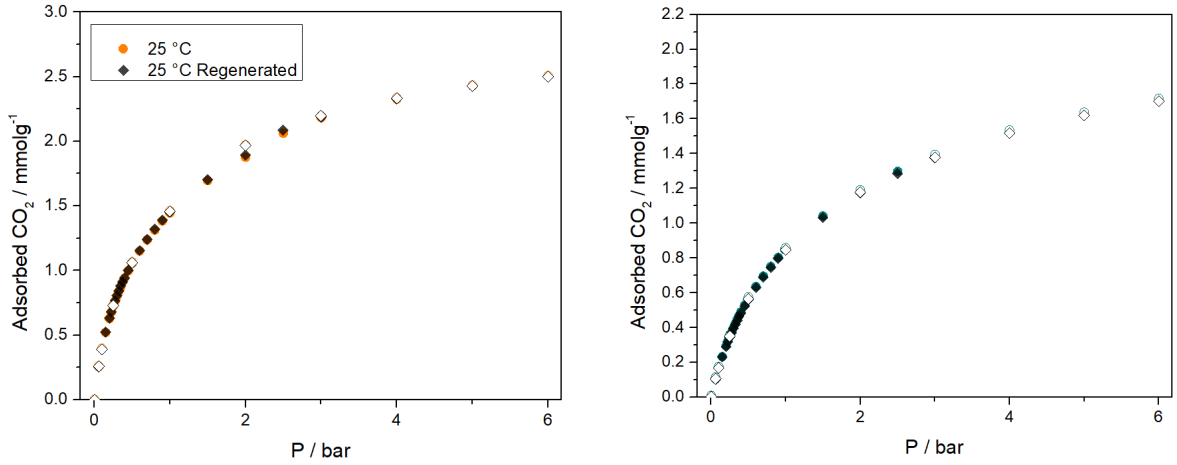


**Figure S23.** Comparison of the high-pressure $CO_2$ adsorption and desorption isotherms of **MUV-26α** and **MUV-26β** at 25 °C before and after temperature cycles, showing complete regeneration.

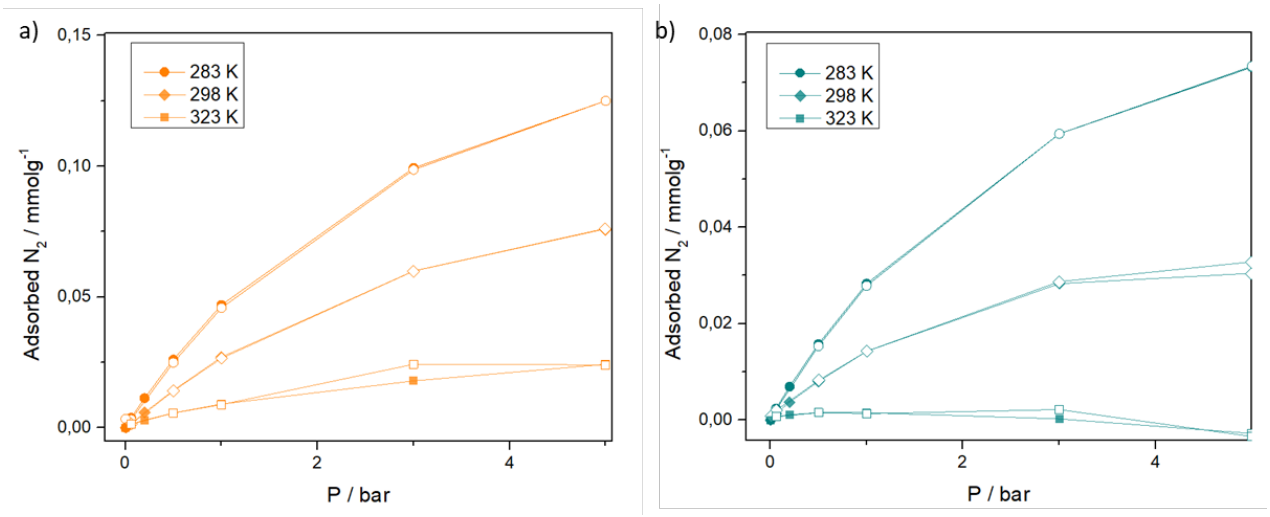


**Figure S24.** Comparison of the high-pressure $N_2$ adsorption and desorption isotherms of **MUV-26α** and **MUV-26β** at different temperatures.

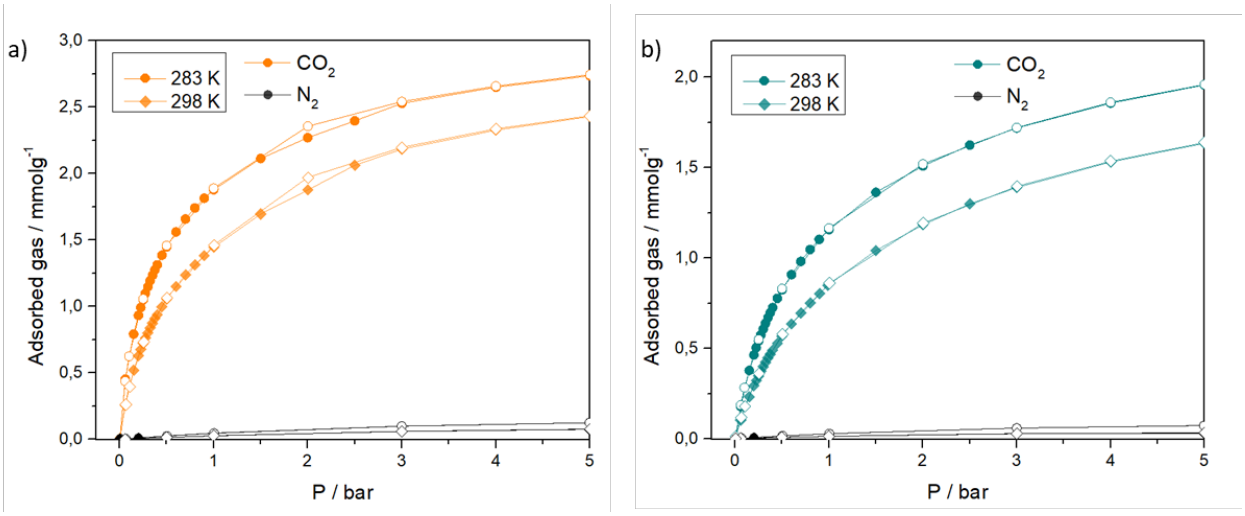


**Figure S25.** Comparison of the high-pressure $CO_2$ and $N_2$ adsorption and desorption isotherms of **MUV-26α** and **MUV-26β** at different temperatures.

### S.4.3.1. Isosteric heat of adsorption

The heat of adsorption was calculated according to the Clausius-Clapeyron equation through the data extracted from the experimental isotherms at different temperatures:

$$q_{st} = R \cdot T^2 \cdot \left[\frac{\delta(lnP)}{\delta T}\right]_{Q=cte} = -R \cdot \left[\frac{\delta(lnP)}{\delta(1/T)}\right]_{Q=cte}$$

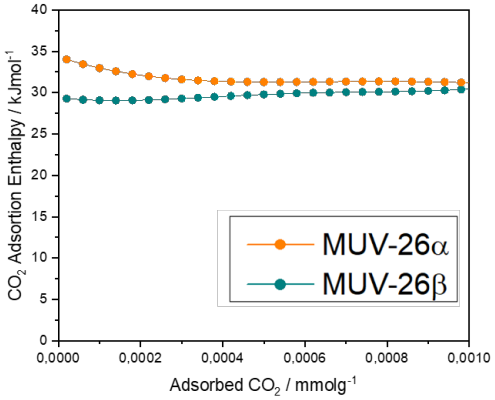


**Figure S26.** Isosteric heat of adsorption of $CO_2$ of **MUV-26α** and **MUV-26β**, leading to an enthalpy of adsorption of 31.4 and 30.4 kJ·mol$^{-1}$, respectively.

### S.4.3.2. Stability after High-pressure $CO_2$ measurements

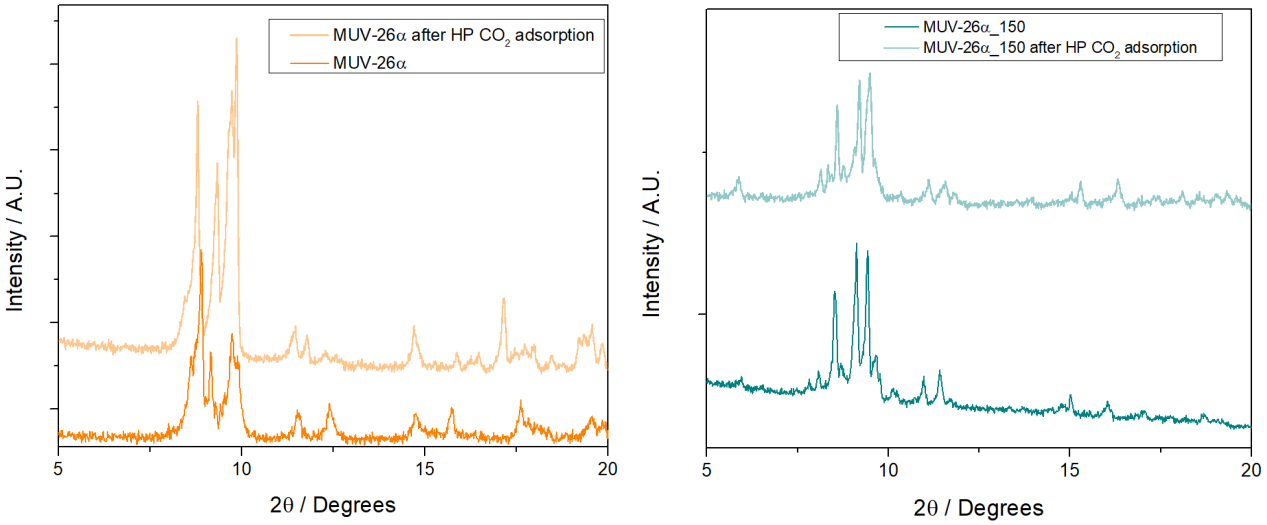


**Figure S27.** Comparison of the PXRD patterns of **MUV-26α** and **MUV-26β** before and after high-pressure $CO_2$ uptake.

## S.5 Separation studies

An ABR (HIDEN Isochema) automated breakthrough analyser setup based on a packed adsorption column was used to determine the adsorption dynamics of pure gases and mixtures. Pressure, temperature and inlet composition can be controlled and tuned for each experiment, and the outlet composition is analysed by an integrated mass spectrometer (HPR-20 QIC). The fixed-bed column was filled either with 374 mg of **MUV-26α** or with 447 mg of **MUV-26β**. Operation conditions ranged 283 K – 323 K, at 1 bar. The inlet stream for the binary mixture was set to a 15 $mL \cdot min^{-1}$ flow of a dilution of $CO_2$ in $N_2$ (5:95; 20:80; and 50:50), simulating realistic industrial mixtures. Time zero was set with the first detection of the trace (1 $mL \cdot min^{-1}$ of He), needed to assure the accuracy of the measurement. In a typical experiment, the sample was regenerated at atmospheric temperature and pressure, in 40 $mL \cdot min^{-1}$ Ar flow for 20 minutes, before each measurement.

$$Selectivity\ (\alpha) = \frac{(quantity\ of\ adsorbed\ CO2)/(Flux\ of\ CO2)}{(quantity\ of\ adsorbed\ N2)/(Flux\ of\ N2)}$$

Given that no nitrogen is adsorbed during the breakthrough experiments, we are reporting the virtually infinite selectivity as >1000.

### S.5.1 $CO_2/N_2$ gas separation

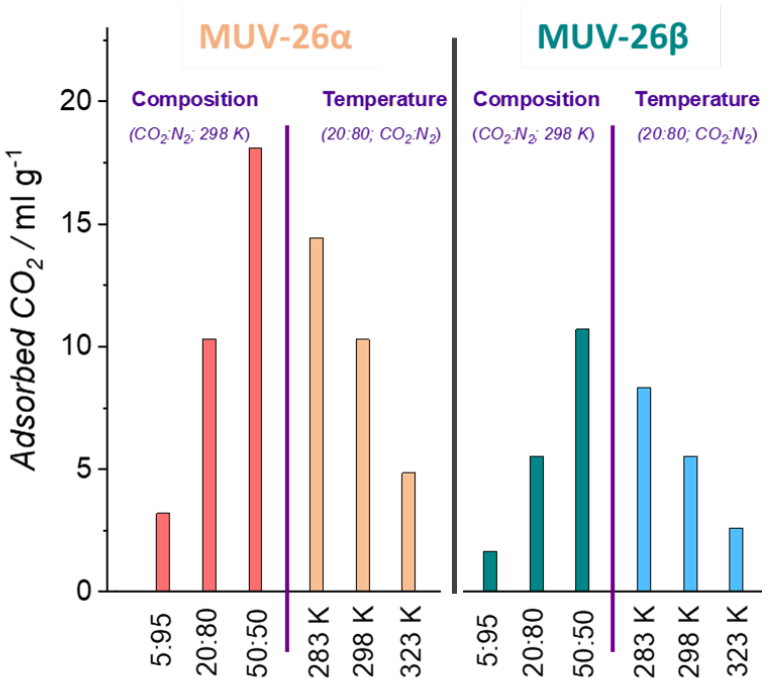


**Figure S28**. Gas adsorbed amounts on **MUV-26**, calculated from breakthrough profiles, at 1 bar (absolute pressure) for $CO_2$:$N_2$ mixtures on: *left*) **MUV-26α**; and, *right*) **MUV-26β**; at different concentrations (5:95; 20:80; and 50:50) and different temperatures (283 K – 323 K). Time zero is set with the first detection of helium (tracer).

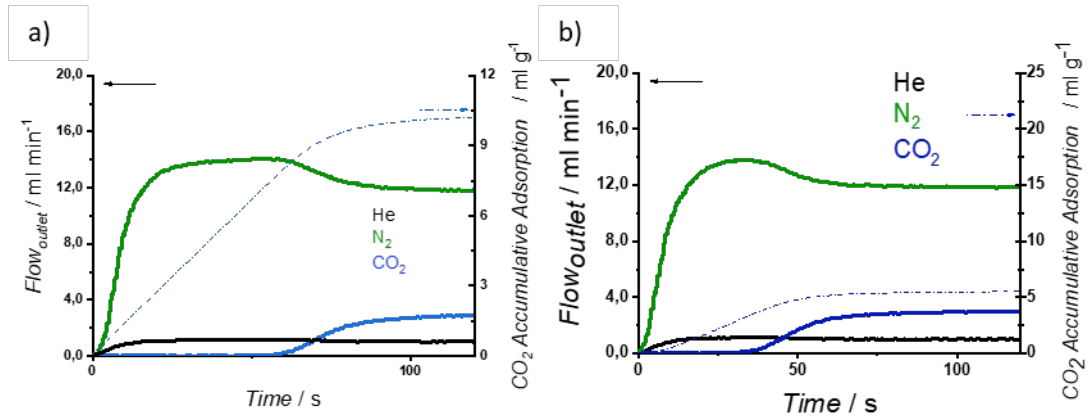


**Figure S29**. Breakthrough exit flowrates (solid line, left axis) and $CO_2$ accumulative adsorption (dash-dot line, right axis) vs. time at **298 K** and 1 bar, on **MUV-26**. Inlet composition corresponds to **20:80** ($CO_2$:$N_2$), on *a*) **MUV-26α**, and *b*) **MUV-26β**. Time zero is set with the first detection of helium (tracer). The total flow rate is 15 ml $min^{-1}$.

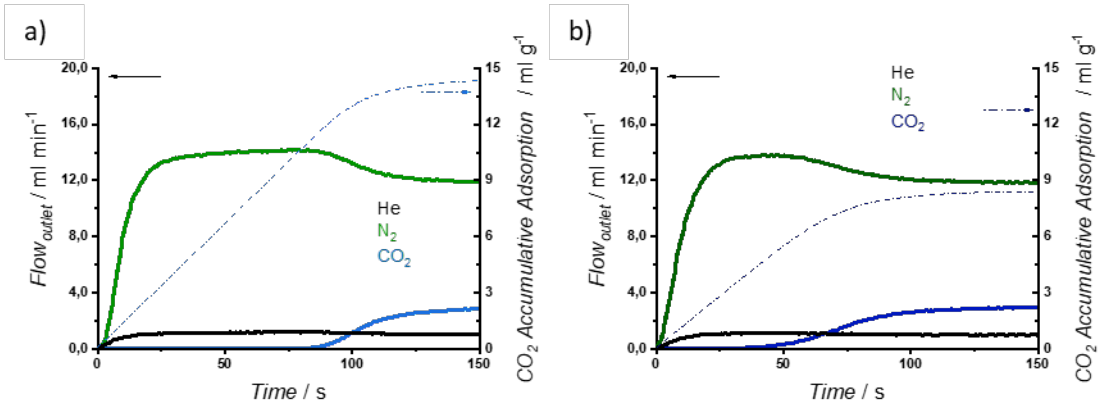


**Figure S30**. Breakthrough exit flowrates (solid line, left axis) and $CO_2$ accumulative adsorption (dash-dot line, right axis) vs. time at **283 K** and 1 bar, on **MUV-26**. Inlet composition corresponds to **20:80** ($CO_2$:$N_2$), on *a*) **MUV-26α**, and *b*) **MUV-26β**. Time zero is set with the first detection of helium (tracer). The total flow rate is 15 ml $min^{-1}$.

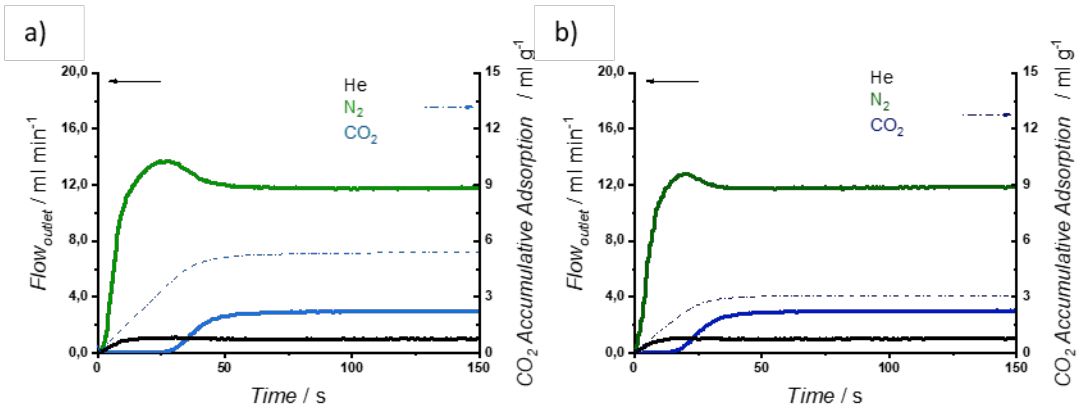


**Figure S31**. Breakthrough exit flowrates (solid line, left axis) and $CO_2$ accumulative adsorption (dash-dot line, right axis) vs. time at **323** K and 1 bar, on **MUV-26**. Inlet composition corresponds to **20:80** ($CO_2$:$N_2$), on *a*) **MUV-26α**, and *b*) **MUV-26β**. Time zero is set with the first detection of helium (tracer). The total flow rate is 15 ml $min^{-1}$.

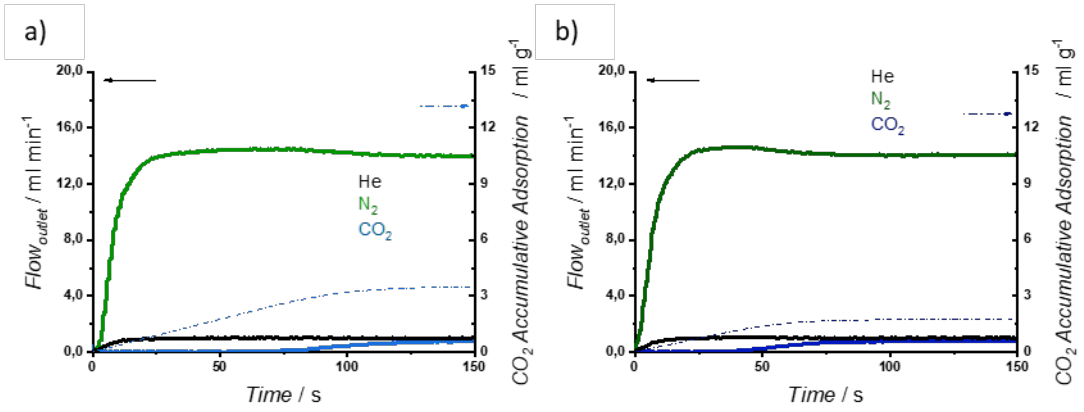


**Figure S32**. Breakthrough exit flowrates (solid line, left axis) and $CO_2$ accumulative adsorption (dash-dot line, right axis) vs. time at **298** K and 1 bar, on **MUV-26**. Inlet composition corresponds to **5:95** ($CO_2$:$N_2$), on *a*) **MUV-26α**, and *b*) **MUV-26β**. Time zero is set with the first detection of helium (tracer). The total flow rate is 15 ml $min^{-1}$.

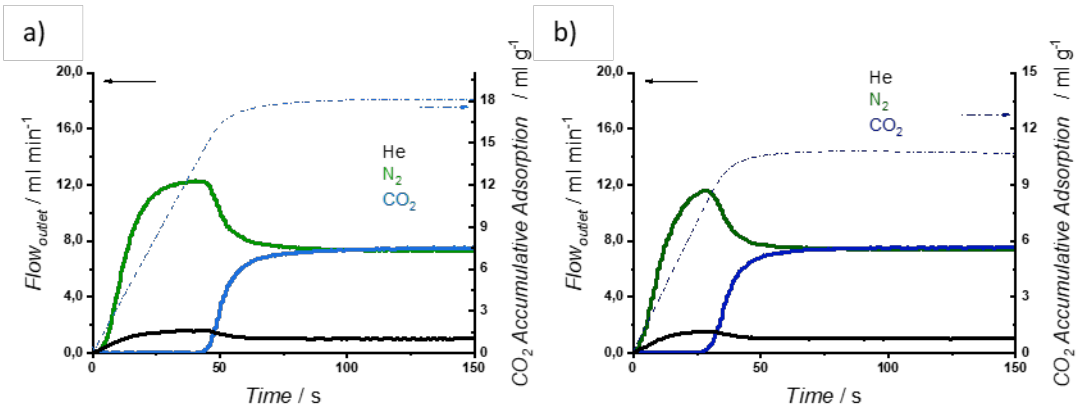


**Figure S33**. Breakthrough exit flowrates (solid line, left axis) and $CO_2$ accumulative adsorption (dash-dot line, right axis) vs. time at **298** K and 1 bar, on **MUV-26**. Inlet composition corresponds to **50:50** ($CO_2$:$N_2$), on *a*) **MUV-26β**, and *b*) **MUV-26α**. Time zero is set with the first detection of helium (tracer). The total flow rate is 15 ml·$min^{-1}$.

In order to probe the complete regeneration achieved on **MUV-26α** at mild conditions (RT, RP, 20 min), each experiment was done with duplicity. In addition, a set of conditions (298 K; $CO_2$:$N_2$, 20:80) was tested in 10 consecutive cycles, to corroborate the stability and high renewability of the sample.

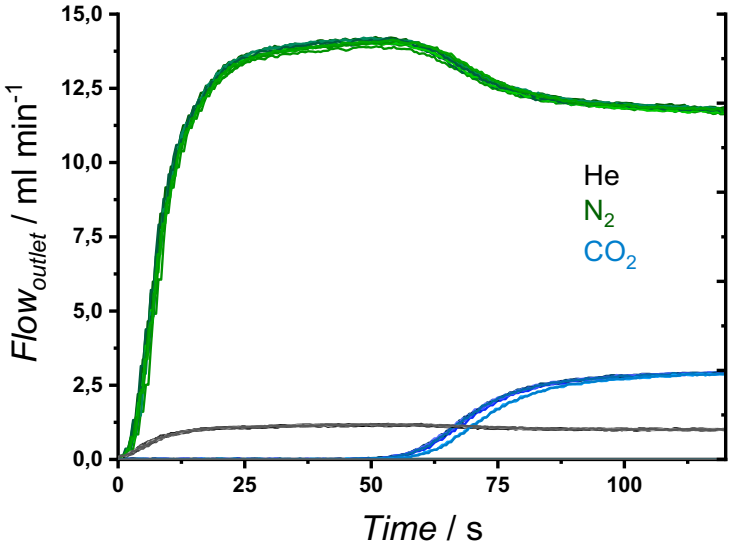


**Figure S34**. Breakthrough exit flowrates (solid line, left axis) and $CO_2$ accumulative adsorption (dash-dot line, right axis) vs. time at **298** K and 1 bar, on **MUV-26α**. Inlet composition corresponds to **20:80** ($CO_2$:$N_2$). Ten consecutive cycles are plotted overlaid. Time zero is set with the first detection of helium (tracer). The total flow rate is 15 ml $min^{-1}$.

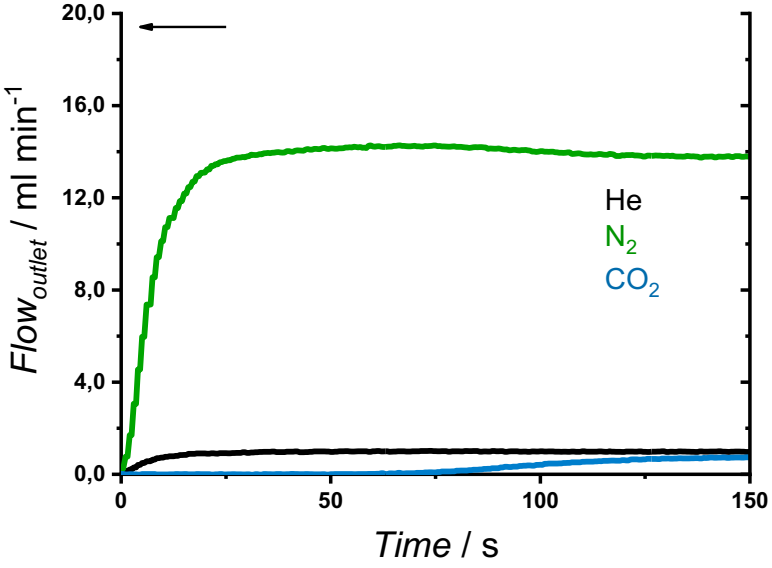


**Figure S35**. Breakthrough exit flowrates (solid line, left axis) and $CO_2$ accumulative adsorption (dash-dot line, right axis) vs. time at 283 K and 1 bar, on **MUV-26α**. Inlet composition corresponds to 5:95 ($CO_2$:$N_2$). Time zero is set with the first detection of helium (tracer). The total flow rate is 15 ml $min^{-1}$.

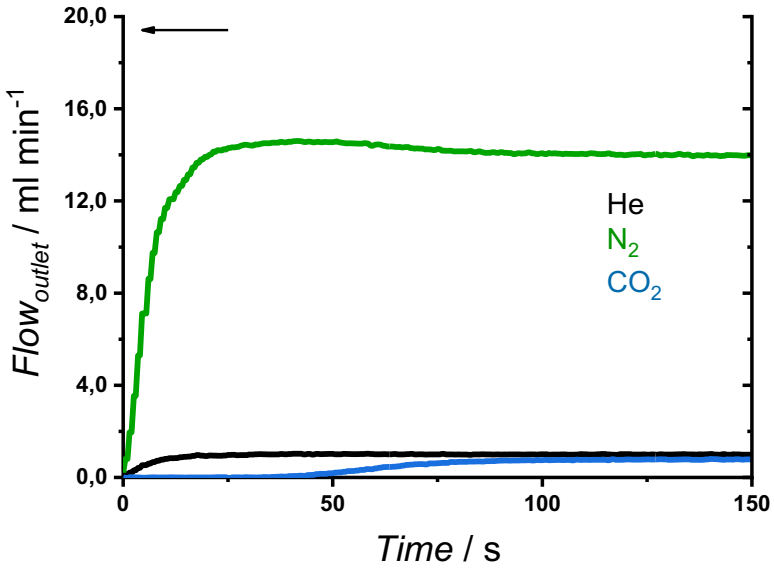


**Figure S36**. Breakthrough exit flowrates (solid line, left axis) and $CO_2$ accumulative adsorption (dash-dot line, right axis) vs. time at 298 K and 1 bar, on **MUV-26α**. Inlet composition corresponds to 5:95 ($CO_2$:$N_2$). Time zero is set with the first detection of helium (tracer). The total flow rate is 15 ml $min^{-1}$.

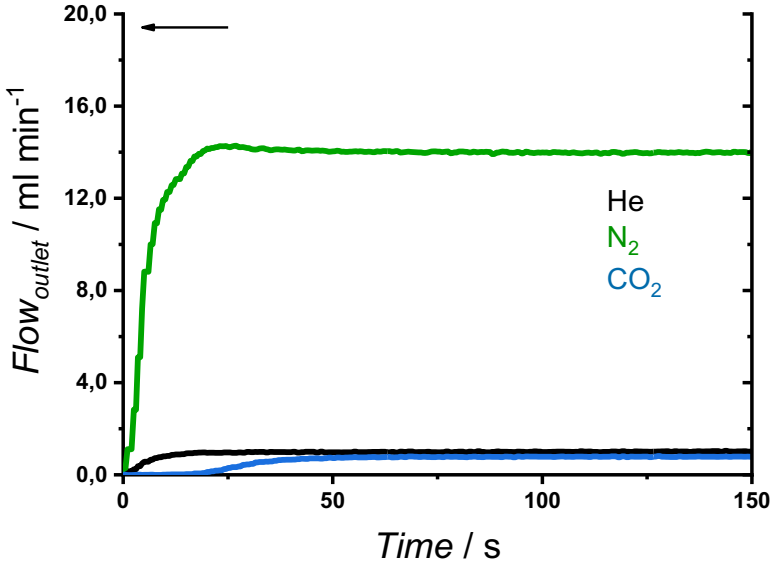


**Figure S37**. Breakthrough exit flowrates (solid line, left axis) and $CO_2$ accumulative adsorption (dash-dot line, right axis) vs. time at 323 K and 1 bar, on **MUV-26α**. Inlet composition corresponds to 5:95 ($CO_2$:$N_2$). Time zero is set with the first detection of helium (tracer). The total flow rate is 15 ml $min^{-1}$.

**Table S9.** Experimental selectivities (α) for **MUV-26**, calculated from the integration of the respective breakthrough curves, from $CO_2$:$N_2$ mixtures, at different concentrations (5:95; 20:80; and 50:50) and different temperatures (283 K - 323 K).

| **MUV-26α** | 5% $CO_2$ ($N_2$) | 20% $CO_2$ ($N_2$) | 50% $CO_2$ ($N_2$) |
|---|---|---|---|
| 283 K | >1000 | >1000 | - |
| 298 K | >1000 | >1000 | >1000 |
| 323 K | >1000 | >1000 | - |
| **MUV-26β** | 5% $CO_2$ ($N_2$) | 20% $CO_2$ ($N_2$) | 50% $CO_2$ ($N_2$) |
| 283 K | - | >1000 | - |
| 298 K | >1000 | >1000 | >1000 |
| 323 K | - | >1000 | - |

**Table S10.** Experimental selectivities (**α**) for **MUV-26α**, calculated from the integration of the respective breakthrough curves, from $CO_2$:$N_2$ mixtures, at different concentrations (5:95; 20:80; and 50:50) and different temperatures (283 K – 323 K).

| | | Flow inlet *(ml/min)* | | | | Adsorbed Amounts *(ml/g)* | | |
|---|---|---|---|---|---|---|---|---|
| % $CO_2$ | T (K) | **$N_2$** | **$CO_2$** | **He** | **Total** | **$N_2$** | **$CO_2$** | **α** |
| 20% | 283 | 12 | 3 | 1 | 16 | n/a | 14.44 | >1000 |
| 20% | 283 | 12 | 3 | 1 | 16 | n/a | 14.45 | >1000 |
| 5% | 298 | 14.2 | 0.8 | 1 | 16 | n/a | 3.24 | >1000 |
| 5% | 298 | 14.2 | 0.8 | 1 | 16 | n/a | 3.01 | >1000 |
| 20% | 298 | 12 | 3 | 1 | 16 | n/a | 10.29 | >1000 |
| 20% | 298 | 12 | 3 | 1 | 16 | n/a | 10.24 | >1000 |
| 20% | 298 | 12 | 3 | 1 | 16 | n/a | 9.63 | >1000 |
| 50% | 298 | 7.5 | 7.5 | 1 | 16 | n/a | 18.11 | >1000 |
| 50% | 298 | 7.5 | 7.5 | 1 | 16 | n/a | 18.44 | >1000 |
| 20% | 323 | 12 | 3 | 1 | 16 | n/a | 4.85 | >1000 |
| 20% | 323 | 12 | 3 | 1 | 16 | n/a | 4.72 | >1000 |
| 5% | 283 | 14.2 | 0.8 | 1 | 16 | n/a | 3.21 | >1000 |
| 5% | 283 | 14.2 | 0.8 | 1 | 16 | n/a | 3.39 | >1000 |
| 5% | 323 | 14.2 | 0.8 | 1 | 16 | n/a | 0.88 | >1000 |
| 5% | 323 | 14.2 | 0.8 | 1 | 16 | n/a | 0.77 | >1000 |

**Table S11.** Experimental gas separation parameters from $CO_2$:$N_2$ mixtures for **MUV-26α.**

| **$CO_2$ concentration** | **T (K)** | **$CO_2$ capacity ($mol \cdot kg^{-1}$)** | **Separation potential ($mol \cdot L^{-1}$)** |
|---|---|---|---|
| **20%** | **283** | 0.64 | 57.78 |
| **20%** | **283** | 0.65 | 57.82 |
| **5%** | **298** | 0.14 | 57.44 |
| **5%** | **298** | 0.13 | 53.51 |
| **20%** | **298** | 0.46 | 41.17 |
| **20%** | **298** | 0.46 | 40.98 |
| **20%** | **298** | 0.43 | 38.54 |
| **50%** | **298** | 0.81 | 18.11 |
| **50%** | **298** | 0.82 | 18.44 |
| **20%** | **323** | 0.22 | 19.39 |
| **20%** | **323** | 0.21 | 18.90 |
| **5%** | **283** | 0.143 | 56.9 |
| **5%** | **283** | 0.151 | 60.1 |
| **5%** | **323** | 0.039 | 15.6 |
| **5%** | **323** | 0.035 | 13.7 |

**Table S12.** Experimental selectivity (**α**) for **MUV-26β**, calculated from the integration of the respective breakthrough curves, from $CO_2$:$N_2$ mixtures, at different concentrations (5:95; 20:80; and 50:50) and different temperatures (283 K - 323 K).

| | | Flow inlet *(ml/min)* | | | | Adsorbed Amounts *(ml/g)* | | |
|---|---|---|---|---|---|---|---|---|
| % $CO_2$ | T *(K)* | **$N_2$** | **$CO_2$** | **He** | **Total** | **$N_2$** | **$CO_2$** | **α** |
| 20% | 283 | 12 | 3 | 1 | 16 | n/a | 8.33 | >1000 |
| 20% | 283 | 12 | 3 | 1 | 16 | n/a | 8.77 | >1000 |
| 5% | 298 | 14.2 | 0.8 | 1 | 16 | n/a | 1.66 | >1000 |
| 5% | 298 | 14.2 | 0.8 | 1 | 16 | n/a | 1.96 | >1000 |
| 20% | 298 | 12 | 3 | 1 | 16 | n/a | 5.52 | >1000 |
| 20% | 298 | 12 | 3 | 1 | 16 | n/a | 5.51 | >1000 |
| 20% | 298 | 12 | 3 | 1 | 16 | n/a | 5.30 | >1000 |
| 50% | 298 | 7.5 | 7.5 | 1 | 16 | n/a | 10.70 | >1000 |
| 50% | 298 | 7.5 | 7.5 | 1 | 16 | n/a | 10.86 | >1000 |
| 20% | 323 | 12 | 3 | 1 | 16 | n/a | 2.59 | >1000 |
| 20% | 323 | 12 | 3 | 1 | 16 | n/a | 2.69 | >1000 |

**Table S13.** Experimental gas separation parameters from $CO_2$:$N_2$ mixtures for **MUV-26β.**

| **$CO_2$ concentration** | **T (K)** | **$CO_2$ capacity ($mol \cdot kg^{-1}$)** | **Separation potential ($mol \cdot L^{-1}$)** |
|---|---|---|---|
| **20%** | **283** | 0.372 | 33.3 |
| **20%** | **283** | 0.392 | 35.1 |
| **5%** | **298** | 0.074 | 29.5 |
| **5%** | **298** | 0.087 | 34.7 |
| **20%** | **298** | 0.246 | 22.1 |
| **20%** | **298** | 0.246 | 22.0 |
| **20%** | **298** | 0.237 | 21.2 |
| **50%** | **298** | 0.477 | 10.7 |
| **50%** | **298** | 0.485 | 10.9 |
| **20%** | **323** | 0.116 | 10.4 |
| **20%** | **323** | 0.120 | 10.7 |

### S.5.2 Stability after gas separation

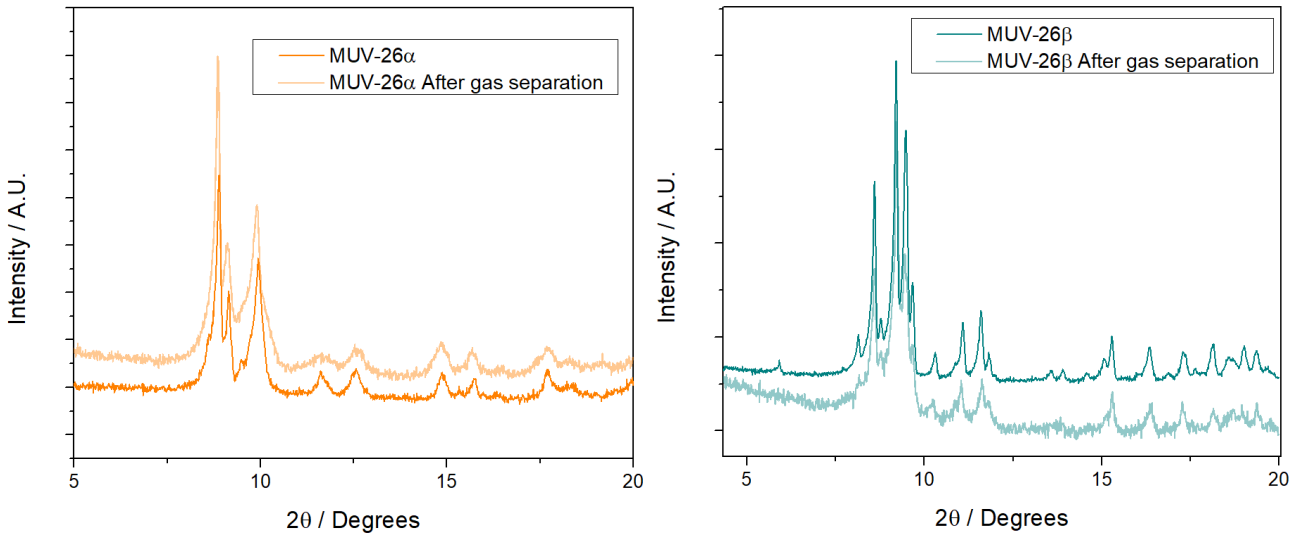


**Figure S38:** Comparison of experimental and simulated PXRD patterns of **MUV-26α** and **MUV-26β** before and after the gas separation experiments, showing retained crystalline structure.

# S.7 References

(1) a) B. N. Figgis and G. B. Robertson, *Nature*, **1965**, *205*, 694–693; b) A. E. Earnshaw, B. N. Figgis and J. Lewis, *J. Chem. Soc. A*, **1966**, 1656–1663.

(2) G. M. Sheldrick, *Acta. Cryst.*, **2015**, *A71*, 3-8.

(3) O. V. Dolomanov, L. J. Bourhis, R. J. Gildea, J. A. K. Howard and H. Puschmann, *J. Appl. Cryst.,* **2009**, *42*, 339-341.

(4) G. J. Long, T. E. Cranshaw and G. Longworth, *Mossb. Effect. Ref. Data J.*, **1983**, *6*, 42.

(5) J.C. Waerenborgh, P. Salamakha, O. Sologub, A.P. Gonçalves, C. Cardoso, S. Sério, M. Godinho and M. Almeida, *Chem. Mater.,* **2000**, *12*, 1743-1749.

(6) N. N. Greenwood, T. C. Gibb, "Mössbauer Spectroscopy" Chapman and Hall, Ltd. Publishers, London (1971)